Transport and drift-driven plasma flow components in the Alcator C-Mod boundary plasma

Citation: Smick, N., B. LaBombard, and I.H. Hutchinson. "Transport and drift-driven plasma flow components in the Alcator C-Mod boundary plasma." Nuclear Fusion 53, no. 2 (February 1, 2013): 023001.

As Published: http://dx.doi.org/10.1088/0029-5515/53/2/023001

Publisher: IOP Publishing

Persistent URL: http://hdl.handle.net/1721.1/84061

Version: Author's final manuscript: final author's manuscript post peer review, without publisher's formatting or copy editing

Transport and drift-driven plasma flow components in the Alcator C-Mod boundary plasma

N. Smick[1] and B. LaBombard[2] and I. H. Hutchinson

Massachusetts Institute of Technology, Plasma Science and Fusion Center
175 Albany St., Cambridge, MA 02139 USA

Boundary layer flows in the Alcator C-Mod tokamak are systematically examined as magnetic topology (upper versus lower-null) and plasma density are changed. Utilizing a unique set of scanning Langmuir-Mach probes, including one on the high-field side midplane, the poloidal variation of plasma flow components in the parallel, diamagnetic and radial directions are resolved in detail. It is found that the plasma flow pattern can be decomposed into two principal parts: (1) a drift-driven component, which lies within a magnetic flux surface and is divergence-free and (2) a transport-driven component, which gives rise to near-sonic parallel flows on the high-field side scrape-off layer. Toroidal rotation, Pfirsch-Schlüter and transport-driven contributions are unambiguously identified. Transport-driven parallel flows are found to dominate the high-field side particle fluxes; the total poloidal-directed flow accounts for ~1/3 to all of the ion flux arriving on the inner divertor. As a result, heat convection is found to be an important player in this region, consistent with the observation of divertor asymmetries that depend on the direction of $\boldsymbol{B} \times \nabla B$ relative to the active x-point. In contrast, the poloidal projection of parallel flow in the low-field scrape-off layer largely cancels with $E_r \times B$ flow; toroidal rotation is the dominant plasma motion there. The magnitude of the transport-driven poloidal flow is found to be quantitatively consistent with fluctuation-induced radial particle fluxes on the low-field side, identifying this as the primary drive mechanism. Fluctuation-induced fluxes on the high-field side are found to be essentially zero, excluding turbulent inward transport as the mechanism that closes the circulation loop in this region.

PACS: 52.30.-q, 52.25.Fi, 52.35.Ra, 52.40.Hf, 52.55.Fa, 52.70.Ds, 52.70.Nc

[1] Presently at Twin Creeks Technologies, Inc, San Jose, CA.
[2] Corresponding Author : Tel. 1-617-253-7264, Fax 1-617-253-0627, e-mail labombard@psfc.mit.edu

1. Introduction

Near-sonic parallel plasma flows are widely observed in the scrape-off layer (SOL) of tokamaks at locations that are far from material surfaces. Such flows are a key component of a tokamak's boundary-layer transport phenomenology, involving a rich interplay among magnetic topology, toroidal plasma rotation, plasma pressure gradients and flow-shear near the last closed flux surface [1]. SOL flows are also found to set a toroidal-rotation boundary condition for the confined plasma [2] and are known to play an important role in the migration of impurities around the plasma periphery (see recent review by Stangeby [3] and references therein).

Extensive measurements of parallel plasma flows have been made in tokamaks [4-24]. A composite picture [23] reveals a persistent flow from the low-field side (LFS) scrape-off layer to the high-field side (HFS) scrape-off layer. These investigations clearly indicate that a ballooning-like transport mechanism is a key contributor to the overall flow pattern. In this scenario, plasma is preferentially lost near the equatorial midplane on the LFS and transits at high velocity along magnetic field lines to 'fill in' the scrape-off layer on the HFS – a region that would otherwise be empty of plasma. This 'filling-in' response is perhaps most dramatically illustrated in double-null magnetic equilibria in which the HFS is magnetically isolated from the LFS. In this case, the HFS scrape-off layer exhibits a pressure e-folding length that is a factor of ~4 smaller than in the LFS scrape-off layer [20]. The behavior has also been clearly identified in plasmas without a magnetic separatrix [21, 24]; when the outermost flux surface is defined by limiter contact on the LFS, the scrape-off layer is thin; when it is defined by contact on the HFS, the scrape-off layer becomes thick. In the later case, parallel flows carry material from the LFS to the HFS. These data indicate that the ballooning-like transport drive is concentrated in a ~30 degree sector about the outer equatorial midplane.

Yet there are some important missing pieces to this flow picture. For diverted plasmas, the level of neutral recycling and ionization at the inner divertor leg does not appear to be sufficient to close the parallel flow circulation loop, i.e., return the material back into the confined plasma at a sufficient rate. This has prompted speculation that an inward convection mechanism may exist on the HFS midplane or divertor leg (e.g. [25, 26]) – perhaps a turbulent transport mechanism, akin to the 'blobs' that are found on the LFS. In addition, transport analysis of CH4 introduced into the DIII-D SOL and its deposition pattern in the inner divertor region suggest that some kind of inward transport mechanism is active there [27, 28].

Another complexity is the role that cross-field drifts ($E_r \times B$ and diamagnetic) play in the overall poloidal flow pattern. When combined with parallel flows, these drifts may reinforce the poloidal circulation or cancel it, resulting in a pure toroidal motion, i.e., no net poloidal circulation. Thus, in order to assess the total poloidal mass flow, one needs to properly account for drift contributions.

Neoclassical parallel flows (Pfirsch-Schlüter) also arise as a consequence of cross-field drifts in a toroidal geometry and may make substantial contributions. Previous experimental investigations have reported detection of Pfirsch-Schlüter flows [13, 22]. However, these analyses were based on simplified models, normally used to estimate the magnitude of Pfirsch-Schlüter flows in closed flux surface regions. Such models do not properly account for toroidal plasma rotation (e.g., see discussion in Ref [29]), which has been found to contribute to parallel flows near the outer midplane with magnitude similar to Pfirsch-Schlüter flows [2].

With the goal of unambiguously resolving these contributions to boundary layer flows, including the role of fluctuation-induced radial particle transport, we have undertaken a detailed experimental investigation in Alcator C-Mod [30]. The key measurements reported here are the three components of plasma flow (parallel, cross-field or 'diamagnetic' and radial) at three different poloidal locations in the plasma, including the HFS midplane. To this end, novel, magnetically-actuated scanning Langmuir-Mach probes were constructed and installed on the tokamak inner wall [31]. These probes have a linear plunge action and a four-electrode, high heat flux handling geometry, similar to existing scanning probes located on the LFS scrape-off layer. Utilizing a series of matched discharges in which the magnetic topology was varied from lower single-null (LSN) to upper-single null (USN), we have been able to unfold the combined contributions of cross-field drifts ($E_r \times B$ and diamagnetic), neoclassical Pfirsch-Schlüter flows, toroidal plasma rotation and fluctuation-induced transport.

A graphical outline of the experimental investigation is shown in Fig. 1. This figure also serves as a table-of-contents for this report. Section 2 describes the arrangement of the plasma flow diagnostics, the techniques used to extract flows and the plasma conditions explored. A direct comparison of flow measurements and their profiles on the LFS and HFS midplanes is assembled in section 3. Here we extract 'transport-driven' and 'drift-driven' components to the net poloidal flow field by comparing LSN and USN topologies. Section 4 analyzes the inferred 'drift-driven' flow component and finds it to be divergence-free as it transits from the LFS to HFS within

magnetic flux surfaces. Thus, this component is consistent with cross-field drift flow ($E_r \times B$ and diamagnetic), lending credibility to the measurements and the techniques used to extract the flows. Within this drift-driven flow field, the Pfirsch-Schlüter component of the parallel flow is readily identified and separated from the parallel flow component that arises from toroidal rotation. The Pfirsch-Schlüter flow pattern is found to transition from the classic dipole structure in the open field line region (which is required to balance vertical grad-B drift flows) to a pattern that cancels with the parallel component of toroidal rotation in closed field line regions. This experimental result is satisfying since it is consistent with theoretical expectations in both regions.

Section 5 examines the transport-driven component of the measured boundary layer flows. A simple particle continuity model is used to compute the required ballooning-like radial flux profiles on the LFS that are needed to account for poloidal flows measured on the HFS. This computation is found to be remarkably consistent, both in its magnitude and profile shape, with direct measurements of the fluctuation-induced particle fluxes on the LFS. Thus we have clearly identified the 'transport' that is responsible for the observed 'transport-driven parallel flows'.

With the source of the transport-driven flow field identified, section 6 turns to the question of the 'sink' mechanism(s) that must close the flow loop, i.e., mechanisms that must bring the mass flux (be it via ions and/or neutrals) back into the confined plasma region. In order to frame the discussion, an extended picture of poloidal plasma flow is assembled, including quantitative measures of particle fluxes arriving on inner and outer divertor surfaces. Over a wide range of divertor plasma conditions (sheath-limited, high-recycling, partially detached), the poloidal projection of the transport-driven flow passing the HFS midplane is found to be of comparable magnitude to the poloidal flow of ions arriving at the inner divertor target. While this behavior might be consistent for low-recycling or detached divertor conditions, it is inconsistent with the expected level of divertor ion flux under high-recycling conditions. This observation implies that an inward plasma transport mechanism must be at play, sending at least a portion of the transport-driven poloidal circulation back into the confined plasma region. Fluctuation-induced radial fluxes are examined at the HFS midplane, looking for this contribution to such an inward-flow closure mechanism. Yet this measurement produces a very robust *negative* result: the fluctuation-induced radial particle fluxes are essentially zero at this location. While this measurement clearly underscores the extreme poloidal asymmetry of fluctuation-induced transport that exists in the

tokamak edge, it does not resolve the flow-loop closure puzzle; it is a topic that must remain open for future studies.

Finally, poloidal heat transport in the HFS scrape-off layer is examined. Parallel convection is found to dominate over parallel conduction in this region regardless of LSN/USN topology. $E_r \times B$ heat convection is also important, being of comparable magnitude to the poloidal component of parallel conduction. Thus, $E_r \times B$ heat convection can inhibit (or enhance) heat flow to the HFS inner divertor leg when $\boldsymbol{B} \times \nabla B$ points to (or away from) the active x-point, leading to a cold (or warmer) inner divertor plasma [32]. This effect provides an explanation, at least in part, for the temperature asymmetries observed in the inner/outer divertor legs that are sensitive to $\boldsymbol{B} \times \nabla B$ direction. It also provides an explanation for some surprisingly low values of electron temperature measured at the HFS midplane the under conditions when the inner divertor is attached, $\boldsymbol{B} \times \nabla B$ points to the active x-point, and the $E_r \times B$ flows away from the inner divertor are large.

2. Experimental Arrangement

Information on Alcator C-Mod's design and overall operation can be found in Ref. [33]. A typical magnetic equilibrium used for the present studies is shown in Fig. 2, along with the locations of scanning and fixed Langmuir probes. The principal diagnostics used for this study are probes: scanning Langmuir-Mach probes at three poloidal locations, including near the LFS and HFS midplanes and divertor target Langmuir probes. Unless stated otherwise, all discharges were ohmic-heated L-modes with toroidal field (B_ϕ) of 5.4 tesla, and plasma current (I_p) of 0.8 MA. In order to unfold the 'drift' and 'transport-driven' components of the flows, otherwise identical sets of matched discharges where run with the last-closed flux surface (LCFS) flipped symmetrically between lower-single null (LSN) and upper-single null (USN). Figure 3 shows example equilibria. This was done with central line-averaged density varying over the range $0.8 \leq \bar{n}_e \leq 1.7\text{x}10^{20}$ m^{-3}, accessing sheath-limited, high-recycling and detached divertor regimes. The influence of the different divertor geometries on the flow pattern (i.e., open upper divertor versus closed lower divertor) was assessed by comparing topologically-identical plasmas with forward and reversed directions of magnetic field. For example, LSN under forward field is compared with USN under reversed field (also LSN-reversed with USN-forward). For the purpose of discussion, magnetic topologies in which $\boldsymbol{B} \times \nabla B$ points from the plasma's magnetic axis towards the active x-point are called 'favorable topologies', in reference to the lower auxiliary power levels needed to access the

H-mode confinement regime. For C-Mod, this corresponds to a LSN configuration with B_ϕ and I_p in the 'forward' direction or a USN configuration with B_ϕ and I_p in the 'reversed' direction.

For a small set of discharges, the upper/lower x-point flux balance was scanned on a shot-by-shot basis from LSN-dominant to USN-dominant, passing through a near-balanced double-null (DN) state. Figure 2 shows an example of this equilibrium.

Data were collected during steady-state periods of ohmic-heated discharges in which plasma current, line-averaged density and magnetic equilibria were held fixed. In a typical discharge, the horizontal, vertical and one of the inner-wall probes were scanned simultaneously a three separate times. These probes 'plunge' all the way to the LCFS with radial velocity of approximately ~ 1 m s^{-1}, dwelling no more than ~3 ms at maximum depth.

Figure 4 shows a close-up view of a robust, high heat-flux handling Langmuir-Mach probe geometry used on all scanning probes [31]. Four tungsten electrodes are embedded in the tip of a molybdenum pyramid structure and labeled according to their compass-point directions: NE, SE, SW and NW. Each electrode projects a cross-sectional area of approximately ~1 mm^2 along magnetic field lines while spreading the incident plasma heat flux over a factor of 2 larger area. This is necessary for C-Mod plasmas, where the parallel heat flux to a material surface exposed to plasma conditions at the LCFS can readily exceed 1 GW m^{-2}.

Typically, all four electrodes are biased with a 2kHz triangular voltage waveform, ranging from -300 to +75 volts with respect to vacuum-vessel ground. Two different data acquisition systems were used to digitally sample the voltage and current signals: a 1 MHz CAMAC-based system (prior to 2008) and a 5 MHz compact PCI-based system. The results reported here are insensitive to the data system used. Current-voltage characteristics obtained by each electrode were fitted using a standard three-parameter offset-exponential function. This produces ion saturation current (I_{sat}), floating potential (V_f) and electron temperature (T_e) at 0.25 ms time intervals. Over this time period, the radial probe movement is typically 0.25 mm or less. Thus plasma density (n), electron temperature, plasma potential (Φ), parallel Mach number ($M_{//}$) and fluctuation-induced radial particle fluxes ($\Gamma_{n,\Phi}$) are recorded over the probe's 'trajectory' through the plasma.

The resultant data from all probes are mapped onto magnetic flux surfaces reconstructed from magnetic measurements [34] and the EFIT plasma equilibrium code [35]. The flux-surface coordinate used here, ρ, is defined as the distance into the SOL along a major radius at the outer

midplane. Smooth spline curves are fit in this ρ-space to data points generated from and in-going and out-going movements of the four electrodes (~400 data points for n, T_e and Φ; ~100 data points for $M_{//}$; ~100 data points for $\Gamma_{n,\Phi}$).

Shifts in the ρ-axis of the probe data are sometimes required in order to 'align' the electron pressure profiles (accounting for ram pressure and kinetic pressure contributions) among the scanning and divertor probes. This required the horizontal probe data to be typically shifted from 1 to 5 mm towards the core plasma (suggesting a systematic offset in EFIT reconstructions), while the inner wall and vertical probes typically require a shift of only ±2 mm and ±1 mm, respectively. In all cases, the shifted horizontal probe data are found to yield an electron temperature profile that is consistent with SOL power balance.

2.1 Parallel flow measurement

Parallel plasma flows are inferred from spatial variations in ion saturation current densities, as recorded on the scanning probe electrodes (NE, SE, NW, SW). The original motivation for employing this four-electrode geometry is that it can operate as a 'Gundestrup'-probe [15, 36], providing information on both parallel and perpendicular components of plasma flow. However, we focus here on only the parallel flows inferred by this four-electrode set. While a generalized theoretical framework for magnetized ion collection by an electrode of arbitrary cross-section is now well developed [37], we have found inconsistencies in the perpendicular flows inferred by this diagnostic [30], even when including diamagnetic corrections and corrections associated with the probe's pyramidal geometry [38]. In contrast, parallel flows measured by this diagnostic are found to be consistent with spectroscopic measurements [1]. In particular, parallel flows inferred from D_β charge-exchange spectra on the HFS midplane [39] are in excellent agreement with parallel flows measured by C-Mod's Inner Wall Langmuir-Mach probes.

In general, ion saturation current collection by an electrode oriented at angle θ with respect to the local magnetic field (within the plane of a flux surface) is given by [37]

$$I_{sat} = eA_p nC_s \exp\left(-1 + M_{\parallel} + M_{\perp}\cot(\theta)\right) \qquad (1)$$

where A_p is the electrode area projected along the magnetic field line, n is the plasma density, C_s is the local sound speed and $M_{\parallel}$, $M_{\perp}$ are the parallel and perpendicular flow Mach numbers (positive flows are directed toward the electrode surface). Since each electrode generates an

independent I-V characteristic, it can report its own local value of I_{sat} and C_s (computed from the local T_e measurement, assuming T_i=T_e). Thus when Eq. (1) is applied simultaneously to all four electrodes, the three unknowns, n, $M_{\parallel}$ and $M_{\perp}$, can be inferred via a least-squares fitting method. This procedure yields parallel Mach numbers that are almost identical to those obtained using a more widely employed semi-empirical formula [40],

$$M_{\parallel} = 0.43 \ln\left(I_{EAST} / I_{WEST}\right). \quad (2)$$

In this case, I_{EAST} and I_{WEST} are the sum of ion saturation currents arriving on the respective east-facing and west-facing electrodes.

2.2 Perpendicular flow measurement

Here we use the term 'perpendicular' to describe flows that are directed across magnetic field lines while lying within a magnetic flux surface (sometimes called the 'diamagnetic direction'). Outside the divertor region, plasma pressure and plasma potential are, to a good approximation, constant on a poloidal flux surface, even flux surfaces that have open field lines. In this context, perpendicular ion flows are dominated by 'drift-flows', which arise from diamagnetic and $E_r \times B$ drifts. These can be simply computed from the radial gradients of plasma ion pressure and potential,

$$\underline{V}_{\perp\, dia} = \frac{\underline{B} \times \nabla_r n T_i}{n B^2}\ , \quad \underline{V}_{\perp\, ExB} = \frac{\underline{B} \times \nabla_r \Phi}{B^2}\ . \quad (3)$$

Using the approximation $T_i \approx T_e$ (all in units of eV in this paper), $V_{\perp\, dia}$ can be computed directly from n and T_e profiles measured by the probes. In order to compute $V_{\perp\, ExB}$, plasma potential profiles must be obtained. These are constructed from Langmuir probe measurements of floating potential (V_f) and electron temperature, accounting for the plasma-probe sheath potential drop, αT_e,

$$\Phi = V_f + \alpha T_e. \quad (4)$$

α is primarily a function of secondary electron emission coefficent, γ_{se}[41]. To account for this, we use tabulated values of γ_{se} for pure tungsten[42] and compute the appropriate value of α for a Maxwellian distribution of primary electrons at the measured temperature, T_e. α varies from 2.8 to 1.4 in a deuterium plasma as T_e ranges from 5 to 100 eV.

The chain of computations and assumptions needed to infer $V_{\perp ExB}$ is the source of some concern, particularly because V_f is typically a large negative value that competes with αT_e. Accurate measures of V_f, T_e and modeling of α is therefore required; yet it is difficult to assess errors in these quantities. Moreover, computing the radial gradient of Φ from profile data leads to significant scatter in the inferred $V_{\perp ExB}$ values. In order to combat this, we take data over many identical discharges and report the average values obtained. Yet, as we shall see, these formulations for $V_{\perp\ dia}$ and $V_{\perp ExB}$ are found to yield an overall ion flow pattern that is remarkably consistent with what is expected for drift-driven flows in the boundary plasma.

2.3 Fluctuation-induced radial particle flux

The four-electrode configuration on the scanning Langmuir-Mach probes (Fig. 4) also provides a measure of fluctuation-induced radial particle fluxes. In general, plasma fluid turbulence leads to transport when density fluctuations and $E \times B$ velocity fluctuations are correlated such that the time-average of their product is non-zero

$$\Gamma_r = \left\langle \tilde{n}\tilde{V}_r \right\rangle = \frac{\left\langle \tilde{n}\tilde{E}_\theta \right\rangle}{B} . \qquad (5)$$

For this measurement, we bias two of the electrodes (NE and SE) with a swept voltage waveform (2kHz triangle wave, -300 to 75 volts). In this way, time-averaged densities and temperatures are measured at these electrode positions by fitting their I-V characteristics. At the same time, ion saturation current fluctuations (sampled at 1 MHz or 5 MHz) are examined during the negative-most portions of the voltage sweeps (corresponding to ~100 μs time segments). Floating potential is simultaneously recorded on the other two electrodes (NW and SW) by leaving them unbiased. Under the assumption that floating potential fluctuations follow plasma potential fluctuations [i.e., electron temperature fluctuations in Eq. (4) can be ignored], the fluctuation-induced radial partial flux, averaged over ~100 μs time segments $\langle ... \rangle$, are computed from

$$\Gamma_r = \frac{\left\langle \tilde{n}\tilde{E}_\theta \right\rangle}{B} = \frac{(n_{NE} + n_{SE})}{2Bd\left\langle \tilde{I}_{NE} + \tilde{I}_{SE} \right\rangle} \left\langle \left(\tilde{I}_{NE} + \tilde{I}_{SE} \right)\left(\tilde{V}_{f\,NW} - \tilde{V}_{f\,SW} \right) \right\rangle . \qquad (6)$$

Here, $\tilde{I}$ and $\tilde{V}$ denote the fluctuating parts with linear trends removed. d is the poloidal spacing of the electrodes, 2.2 mm. Approximately equal radial fluxes are obtained if NW and SW electrodes

are used instead for I_{sat} collection (NE and SE floating). 1 MHz or 5 MHz digital sampling rates also give similar results.

Earlier investigations in C-Mod identified inconsistencies in radial fluctuation-induced particle fluxes measured by previous Langmuir-Mach probe designs [43]. Most notable among these was: (1) a radial flux density at the outer midplane that was a factor of ~10 higher than that expected from global particle balance (assuming poloidal symmetry in particle transport) and (2) a measurement of a radial flux density that continued to increase as the probe passed well inside the last-closed flux surface. Concern was raised that the probe body might be interfering with the flux measurements; radial flux induced by the presence of the probe head might compete with the radial flux that is present in the unperturbed plasma. The probe design of Fig. 4 aims to avoid this effect: the four electrodes are placed at the tip of the probe body rather than recessed behind a limiter-like pyramidal structure. This improvement, combined with the realization that most of the particle loss may in fact be occurring over a narrow poloidal sector about the outer midplane (i.e., ~1/10th of the plasma boundary area), yields fluctuation-induced radial particle fluxes at LFS midplane that are quantitatively consistent with 'transport-driven' parallel plasma flows observed in at HFS midplane (section 5.2). Moreover, fluctuation-induced radial particle fluxes measured at the HFS midplane are found to be essentially zero – direct evidence of the extreme poloidal asymmetry in radial transport and supporting evidence that probe-perturbation effects on Γ_r measurements might be ignorable.

3. Flow profile measurements

First we examine radial profiles of parallel and perpendicular flow velocities obtained from the inner-wall and horizontal scanning probe systems. These profiles were produced by averaging data obtained from multiple discharges, all with toroidal field (B_ϕ) of 5.4 tesla, plasma current (I_p) of 0.8 MA and line-averaged densities spanning the range $0.8 < \bar{n}_e < 1.7\text{x}10^{20}$ m^{-3}.

3.1 Net poloidal flow profiles on LFS and HFS

Figure 5 shows poloidal projections of parallel and perpendicular flow velocities ($E_r \times B$) and the resulting net poloidal flow velocities. Positive velocities indicate flow directed toward the inner divertor. These data were obtained from the HFS and LFS midplane scanning probes with

favorable and unfavorable $B \times \nabla B$ drift directions (i.e., $B \times \nabla B$ directed toward and away from the active x-point, respectively). Since there are two ways to get favorable topologies (LSN, normal field and USN, reversed field) and two ways to get unfavorable topologies (USN, normal field and LSN, reversed field), there are four possible flow patterns to investigate. However, without any external momentum input and with the exception of differences in divertor geometry, we expect the two favorable cases should yield identical flow patterns, as should the two unfavorable cases. Displayed in this plot are the favorable and unfavorable cases with the largest data set, i.e, that obtained with normal field direction. We see a complex behavior, which is different for the two poloidal locations and different for the two $\boldsymbol{B} \times \nabla B$ drift directions. Net poloidal flow on the HFS is dominated by the parallel flow contribution and is always directed toward the inner divertor. In contrast, net poloidal flow on the LFS involves a balance between parallel flows and ($E_r \times B$) flows. These destructively interfere in the open field line region ($\rho > 0$) but reinforce in the closed field line region. In order to unfold this picture in more detail, we now use magnetic topology variation as a tool to identify underlying symmetries in the data and to extract 'transport-driven' and 'drift-driven' flow components.

3.2 Transport and drift-driven flow components

We use the term 'transport-driven flows' to describe flows that arise in response to poloidal transport asymmetries. Such asymmetries require strong parallel flows in the boundary layer to maintain particle continuity [2]. Since these flows do not depend on the sign of the magnetic field, their direction should depend only on which x-point is active, that is, whether the magnetic topology is LSN or USN. In contrast, we use the term 'drift-driven flows' to describe flows that depend on the sign of B and therefore change with field direction, not with magnetic x-point topology. Perpendicular drift-driven flows include diamagnetic and $E_r \times B$ flows. Drift-driven flows in a toroidal geometry also produce parallel flows, e.g., Pfirsch-Schlüter flows [44]; these are required to make the overall drift-driven flow pattern divergence-free. Drift-driven parallel flows also arise if the plasma exhibits a pure toroidal rotation – these are the parallel flows required to cancel the poloidal component of $E_r \times B$ drift. In a reference frame rotating toroidally with the plasma motion, the radial electric field is zero. An example of this cancellation between poloidal components of $E_r \times B$ and parallel flow is seen in the LFS data of Fig. 5 for $\rho > 3$ mm. These flow-

drive mechanisms and their expected symmetry properties with respect to the sign of B (drift-driven) or x-point topology (transport-driven) are summarized in Table 1.

Table 1: Flow components and their symmetries with respect to field reversal and x-point topology.

	Parallel Flow	**Perpendicular Flow**
Drift-driven flow (depends on sign of *B*)	Pfirsch-Schlüter flow || Component of toroidal rotation	$E_r \times B$ Drift Diamagnetic drift
Transport-driven flow (depends on LSN/USN)	Transport-driven || flow	Transport-driven toroidal rotation (indirectly affecting $E_r \times B$)

Utilizing measurements of parallel and perpendicular flows under field reversal and x-point topology variation, it is possible to uniquely identify the individual flow contributions in the four quadrants of Table 1. This technique has been used previously in Ref. [2] to examine *parallel* flow measurements and identify transport-driven and drift-driven contributions. Here we apply it for the first time to the combined set of parallel and perpendicular flow measurements obtained in the LFS and HFS scrape-off layers.

In preparation for this task, Fig. 6 shows the poloidal projections of the measured parallel and perpendicular flows in a different format. Unlike in Fig. 5, the parallel components for favorable and unfavorable drift directions are over-plotted and color-coded according to LSN/USN topologies and field directions (top panels). The perpendicular flows are grouped together in a similar manner (bottom panels). Data from reversed-field USN/LSN comparison experiments are also shown (LFS only). The sign convention used here is that flow towards the inner divertor is assigned a positive value. This means that the coordinate system in physical space actually flips with the location of the x-point (USN vs. LSN), i.e., the poloidal and toroidal coordinates change sign. Thus, transport-driven flows are expected to maintain the same sign when going from favorable to unfavorable geometries, i.e., they are 'symmetric' with respect to this change. In contrast, drift-driven flows are expected to change sign in going from favorable to unfavorable geometries; they are 'anti-symmetric' in this coordinate system. A similar decomposition of edge plasma flows into two symmetry groups has also been employed by Catto and Simakov [45, 46].

With this coordinate system convention, the symmetric (transport-driven) and anti-symmetric (drift-driven) velocity components can be extracted by simply taking the sum and difference of the data from favorable and unfavorable topologies:

$$V_{sym} = (V_{fav} + V_{unfav})/2$$
$$V_{anti-sym} = (V_{fav} - V_{unfav})/2 \quad (7)$$

These are shown in Fig. 7. In principle, symmetric and anti-symmetric components can be produced independently from any pair of favorable and unfavorable velocity measurements. Displayed for the LFS data are the results of two different pairings: the blue/red curves show the result of USN/LSN topology reversal in normal field, while the purple/orange curves show the result of field reversal in LSN topology. On the HFS, no reversed-field data are available, so only data from topology reversal in normal field are shown. Positive values of symmetric component indicate flow towards the inner divertor; positive values of anti-symmetric component indicate flow in the electron diamagnetic drift direction. Thus, regardless of how the symmetric/anti-symmetric components are deduced (e.g., USN compared to LSN, forward compared to reversed B), we should expect them to exhibit the same magnitude and sign. We see that the blue/purple and red/orange curves on the LFS do indeed overlay very well, which indicates the rough equivalence of field and topology reversal experiments. That is, we cannot detect any significant effect due to differences in C-Mod's upper versus lower divertor geometry or the fact that the probes are not located precisely on the LFS/HFS midplanes.

The result of these manipulations is that we have extracted the anti-symmetric (drift-driven) and symmetric (transport-driven) parts of the parallel and perpendicular contributions to the poloidal flow. These components can be further examined in terms of the underlying drive mechanisms listed in Table 1. The dominant term in the LFS scrape-off layer is an anti-symmetric, parallel (drift-driven) component in the electron diamagnetic direction. On the HFS, the largest contributor to the poloidal flow is a symmetric, parallel (transport-driven) flow component towards the inner divertor. Since the perpendicular contributions are smaller, these findings are in agreement with the original flow picture that was developed initially from measuring parallel flows alone. However, the perpendicular contributions, while smaller, are not negligible.

In the LFS scrape-off layer, the anti-symmetric (drift-driven) and symmetric (transport-driven) components sum constructively for favorable drift direction and destructively for unfavorable drift direction. This is true for both parallel and perpendicular components. This tends to produce larger (or smaller) poloidal flow velocities in favorable (or unfavorable) drift topologies and thus may influence overall transport levels via differences in flow shear [1].

It is also interesting to note that the symmetric (transport-driven) flow components measured on the LFS, though small, amount to a nearly perfect toroidal rotation (see upper-right panel of Fig. 7). The parallel and perpendicular contributions are approximately equal and opposite, resulting in a net zero poloidal flow. The resultant symmetric (transport-driven) toroidal velocity has a maximum of about 3 km/s and is co-current directed under favorable drift conditions and counter-current directed in unfavorable conditions (see Fig. 8).

Measurements inside the last-closed flux surface (LCFS, $\rho = 0$) on the LFS indicate that anti-symmetric (drift-driven) perpendicular flows are the dominant contributor to poloidal flows there (see right panels in Fig. 7). Moreover, this perpendicular flow component reverses direction from ion diamagnetic direction outside the LCFS ($\rho > 0$) to electron diamagnetic direction inside ($\rho < 0$). This result agrees with the expectation that E_r points outward on open field lines and inward on closed field lines. On open field lines, the plasma potential is roughly proportional to the electron temperature, owing to sheath potential drops at the divertor target ($\Phi \sim 3\,T_{e,div}$) combined with the thermal gradient force in the electron parallel momentum equation ($\Phi \sim 0.71\,T_e$). [Note: The potential variation along field lines occurs primarily in the divertor region.] On closed field lines, E_r points inwards such that the $E_r \times B$ drift partially cancels the ion diamagnetic drift to reduce both poloidal and toroidal ion velocities.

Turning our attention to the flows measured on the HFS midplane (left panels in Fig. 7), we see that the symmetric (transport-driven) parallel flow component is the dominant contributor to the poloidal flow. All other poloidal flow components are significantly smaller. The anti-symmetric (drift-driven) perpendicular component shows a slight tendency toward the electron diamagnetic direction in the vicinity of the separatrix and is slightly in the ion diamagnetic direction elsewhere. This is reminiscent of the behavior on the LFS, but much weaker.

Symmetric (transport-driven) parallel flows on the HFS are observed to increase in magnitude with distance from the LCFS. This is consistent with the idea that a ballooning-like transport asymmetry is the primary drive mechanism: starting from nearly poloidal symmetric pressure profile at the LCFS, plasma transports rapidly into the SOL predominantly on the LFS midplane. This results in poloidal pressure asymmetries that become stronger with depth into the SOL and hence stronger transport-driven parallel flows.

4. Analysis of drift-driven flow field

Cross-field drift flows and drift-driven parallel flows in the tokamak geometry are well understood and described by basic theory. Having isolated the drift-driven and transport-driven flow components, we can test if the drift-driven part is consistent with these expectations. If found consistent, we can then proceed with confidence that our flow measurement techniques are reliable and that the transport-driven component is being correctly characterized.

4.1 Divergence-free flow requirement

The classical fluid drifts under consideration here ($E_r \times B$ and ion diamagnetic) can be written in terms of gradients of flux functions, $\Phi(\psi)$ and $p_i(\psi)$ {see Eq. (3)}, in regions where these quantities are approximately constant on a flux surface, i.e., on closed magnetic field lines or on open magnetic field lines at locations that are sufficiently far away from limiter/divertor surfaces. These are the situations that are being considered here. In this case, the fluid drift fluxes lie strictly within a flux surface; fluid drifts in the 'radial' direction are zero. {As a reminder, we use the term 'radial' to refer to vectors that are perpendicular to flux surfaces. We use the term 'perpendicular' to refer to vectors that are both perpendicular to the magnetic field and lie within a flux surface.} With the radial flow and its divergence being zero, the remaining drift-driven plasma fluid flow field must be expressible in the form [47],

$$n\underline{V}_d = n\Omega(\rho)R\hat{\phi} + C(\rho)\underline{B} \ , \qquad (8)$$

in order to be divergence-free. The first term on the right of Eq. (8) allows for a toroidal plasma rotation (from diamagnetic and $E_r \times B$ drift contributions in the toroidal direction, $\hat{\phi}$) with a constant angular frequency, Ω, which may be function of flux surface (ρ). {For convenience, we label flux surfaces by their distance into the SOL at the outer midplane, ρ.} The second term accounts for plasma flow along magnetic field lines, with a magnitude that is a flux-function constant, $C(\rho)$, times the local magnetic field strength.

4.2 $E_r \times B$ Toroidal Rotation and Pfirsch-Schlüter Flows

Taking the poloidal projection of Eq. (8), we see that in order for the flow to be divergence-free the drift-driven poloidal flux density on a given flux surface must be equal to the constant $C(\rho)$ times the local poloidal magnetic field strength,

$$\left.\frac{nV_{d,\theta}}{B_\theta}\right|_\rho = C(\rho). \tag{9}$$

Recognizing that the total drift-driven poloidal flux density is the sum of perpendicular (diamagnetic and $E_r \times B$, $nV_{d,\perp}$) and parallel (e.g., Pfirsch-Schlüter, $nV_{d,//}$) components,

$$nV_{d,\theta} = nV_{d,//}\frac{B_\theta}{B} + nV_{d,\perp}\frac{B_\phi}{B}, \tag{10}$$

we now see the 'drive' mechanism for drift-driven parallel flows. If the poloidal projection of the $nV_{d,\perp}$ term does not by itself satisfy Eq. (9) then parallel flows must arise ($nV_{d,//}$) so that the total poloidal flow does satisfy Eq. (9). These two constraints yield an explicit formula for the drift-driven parallel flow on a given flux surface, ρ,

$$nV_{d,//} = C(\rho)B - nV_{d,\perp}\frac{B_\phi}{B_\theta}\ . \tag{11}$$

If we pick a value of $C(\rho)$ such that $nV_{d,//}$ is zero at the top of a toroidal plasma, then $nV_{d,//}$ will be zero at the bottom (if the plasma is top-bottom symmetric) and, owing to the $1/R$ variation in toroidal magnetic field strength, $nV_{d,//}$ will have a $\sim\cos\theta$ modulation with respect to poloidal angle. Such a spatially-modulated parallel flow pattern is generally called a 'Pfirsch-Schlüter parallel flow' after the original discoverers of an analogous effect that modulates parallel currents in toroidal geometry[44]. However, unlike in the case of parallel currents, the term 'Pfirsch-Schlüter' can be ambiguous when used to describe parallel ion flows. This is because the local magnitude of $nV_{d,//}$ depends on the toroidal rotation of the plasma with respect to the measurement frame. (In Ref [29], this ambiguity is also noted as a need to specify a boundary condition on the total parallel flow, $nV_{d,//}$.) In order to avoid this ambiguity, we perform a Galilean transformation on our anti-symmetric (drift-driven) flow data to a reference frame that is rotating with the plasma's toroidal angular velocity, ω. In this frame, the radial electric field is zero. Noting that a Galilean transformation must satisfy $\underline{E} + \underline{V} \times \underline{B} = 0$, the appropriate toroidal rotation velocity for this frame is $V_{rot} = E_r / B_\theta$, or

$$\omega = \frac{V_{rot}}{R} = \frac{E_r}{RB_\theta} = -\frac{\nabla\Phi}{RB_\theta} = -2\pi\frac{\nabla\Phi}{|\nabla\psi|} = -2\pi\frac{\partial\Phi}{\partial\psi}. \tag{12}$$

Thus ω is a flux function that essentially encodes the radial structure of E_r seen in the lab frame. Having effectively subtracted the $E_r \times B$ toroidal rotation, the Pfirsch-Schlüter flow then can be

clearly identified as the parallel component seen in the rotating frame. A graphical illustration of this vector decomposition process is shown in Fig. 9. Thus, the total drift-driven parallel flow in the lab frame is the sum of Pfirsch-Schlüter ion flow and the parallel component of toroidal plasma rotation.

4.3 Consistency tests

The measurements of drift-driven parallel flow, $E_r \times B$ flow and ion diamagnetic flow can be used to compute the total drift-driven ion fluid velocity at both the HFS and LFS midplane locations. The poloidal projection of these fluid velocities can then be used to compute two flow parameters: $C(\rho)$ {using Eq. (9)} and $\omega(\rho)$ {using Eq. (12)}, as a function of flux surface coordinate. If our measurements are consistent with divergence-free poloidal flow, these parameters should exhibit the same profile on the HFS and LFS, i.e., they should behave as flux functions. The measured parallel flow can also be decomposed into toroidal rotation and Pfirsch-Schlüter ion flow contributions. The primary caveat in this calculation is the lack of a direct ion pressure gradient measurement. We assume that the ion pressure gradient is equal to the electron pressure gradient, but this should be viewed as a convenient approximation. While measurements show that impurity ion and electron temperatures tend to be similar in the pedestal region [48] (as expected for the high collisionality of C-Mod edge plasma), preliminary measurements of T_i in the scrape-off layer indicate that they may be factor of ~2-3 larger than T_e and exhibit a longer e-folding length [49]. The impact of these observations on the analysis performed here will need to be assessed in future work.

Figures 10 and 11 show the result of performing this procedure to the anti-symmetric (drift-driven) flow components, which were extracted from topology-reversal experiments with normal field direction (data shown in lower panels of Fig. 7). The decomposition of the flow vectors is shown in Fig. 10; the resultant poloidal flow and toroidal rotation parameters {$C(\rho)$ and $\omega(\rho)$} are shown in Fig. 11.

Several important observations can be made from these figures:

1. $\omega(\rho)$ is well matched between LFS and HFS data. This result is consistent with plasma potential mapping along field lines from the low to high-field sides, i.e., the measured potential profile behaves as a flux function. The observed $E_r \times B$ toroidal rotation peaks at ~5 km/s in the co-current direction near ρ = ~3 mm in the SOL, reverses direction near the

LCFS and reaches ~20 km/s in the counter-current direction near ρ = -2 mm in the confined plasma.

2. $C(\rho) = nV_{d,\theta}/B_\theta$ is also well matched between the LFS and HFS locations, indicating that the anti-symmetric (drift-driven) flow field identified in Fig. 7 is a divergence-free poloidal flow field. This is true despite the clear differences in radial structure of the various flows components at the two locations.
3. The largest contributor to the net poloidal fluid velocity is the ion diamagnetic velocity, but the parallel flow and the $E_r \times B$ flow contribute significantly as well. The resultant $V_{d,\theta}$ is peaked near the LCFS in the ion diamagnetic direction and has a maximum value of ~4 km/s. $V_{d,\theta}$ approaches zero inside the LCFS at $\rho \sim$ -3 mm and also in the far SOL a $\rho \sim$ 10 mm. This is direct confirmation that the diamagnetic and $E_r \times B$ drifts tend to cancel in the closed field line region.
4. The measured drift-driven $V_{d,\parallel}$ in the LFS SOL has similar contributions from Pfirsch-Schlüter flow and $E_r \times B$ toroidal rotation. Inside the LCFS and in the HFS SOL, the two components tend to cancel. Note that in the far SOL of both the HFS and LFS where the net $V_{d,\theta}$ is near zero, the familiar $\cos\theta$ behavior of the Pfirsch-Schlüter flow is recovered, i.e., opposite flow directions are observed on the HFS and LFS. Near the LCFS however, where $V_{d,\theta}$ is finite, the Pfirsch-Schlüter flow is in the same direction at both locations.

It should be noted that others have attempted to explain LFS parallel flow measurements in terms of drift-driven flows [13, 22]. Most notably, Pitts *et al.* [22] measured parallel flow at the LFS midplane on TCV in detail for forward and reversed field cases. Over a wide range of densities the parallel flow was found to largely reverse with field direction, indicating that drift-driven flows dominate in this region. Estimates of the expected Pfirsch-Schlüter parallel flow based on a simple $\sim\cos\theta$ modulation formula were found to compare favorably with experimental measurements [13, 22]. However, these analyses did not take into account the possible contribution of toroidal plasma rotation.

In summary, we find that the anti-symmetric (drift-driven) flow field that has been extracted from topology reversal experiments (Fig. 7) satisfies basic consistency tests: Plasma potential is approximately a flux function and the total ion flow within the flux surface is divergence-free. This

result is intellectually satisfying and lends confidence to the flow measurement techniques. We now turn attention to the other half of the flow picture, that of transport-driven flows.

5. Analysis of transport-driven flow field

Unlike the anti-symmetric (drift-driven) flow field, the symmetric (transport-driven) flow field has a poloidal divergence that is *not* zero. This is seen by inspection of Fig. 7: the net poloidal flow on the LFS is negligible compared to the ~2 km/s flow on the HFS. The presumption is that the transport-driven poloidal flow arises so as to balance ballooning-like radial transport fluxes. In order to test this hypothesis, we adopt a simple model for the poloidal variation in radial transport such that the radial particle flux density profile (nV_r) at the LFS midplane can be quantified. This estimate of nV_r is then compared to direct measurements of fluctuation-induced radial particle flux profiles at the LFS midplane. In short, we find that the symmetric (transport-driven) flow field does indeed satisfy this consistency test – the measured radial transport is of appropriate magnitude to quantitatively explain the observed transport-driven poloidal flow.

5.1 Particle continuity analysis

The transport-driven flow field, $n\underline{V}_{tr}$, is expected to satisfy a divergence requirement that involves both poloidal and radial particle fluxes,

$$\nabla\cdot n\underline{V}_{tr} = \nabla_r\cdot n\underline{V}_{tr,r} + \nabla_\theta\cdot n\underline{V}_{tr,\theta} = 0. \qquad (13)$$

Note that the poloidal divergence term can be written as

$$\nabla_\theta\cdot\frac{nV_{tr,\theta}}{B_\theta}\underline{B}_\theta = \frac{nV_{tr,\theta}}{B_\theta}\nabla_\theta\cdot\underline{B}_\theta + \underline{B}_\theta\cdot\nabla_\theta\frac{nV_{tr,\theta}}{B_\theta} \approx \underline{B}_\theta\cdot\nabla_\theta\frac{nV_{tr,\theta}}{B_\theta}.$$

Thus, as in Eq. (9), the poloidal divergence will be non-zero when the quantity $nV_{tr,\theta}/B_\theta$ varies with poloidal angle.

We begin by assuming that all the radial transport is localized to the LFS. This assumption is consistent with our observations of ballooning-like transport asymmetry in C-Mod [2, 20] as well as similar observations in other experiments. Experiments by Gunn *et al*. on Tore Supra [21] revealed strong transport-driven parallel flows caused by a ballooning-like particle source localized to within a 30° sector centered at the LFS midplane. In this case, we expect $nV_{tr,\theta}/B_\theta$ to vary in poloidal angle, particularly near the outer midplane, as it accommodates the ballooning-like

poloidal asymmetry in radial transport. To capture this effect, we model $nV_{tr,\theta}/B_\theta$ as a sinusoid in the LFS region, transitioning to constant value on the HFS,

$$\frac{nV_{tr,\theta}}{B_\theta} = \begin{cases} k(r)\sin\theta & ; \ |\theta| \le \pi/2 \\ k(r) & ; \ \theta > \pi/2 \end{cases} . \qquad (14)$$

$k(r)$ contains the radial structure of $nV_{tr,\theta}/B_\theta$; r is the plasma minor radius at the LFS midplane; θ is poloidal angle measured from the LFS midplane. The amplitude of the sine function, *k(r)*, coincides with the measured radial profile of $nV_{tr,\theta}/B_\theta$ at the HFS midplane.

In order to satisfy Eq. (13), the radial flux must have a non-zero radial divergence that is a function of poloidal angle. This situation is illustrated in Fig. 12. Note that since this flow field is entirely transport-driven, neutral ionization sources are not included, i.e., the total divergence of the flow field is set to zero. While a significant level of local ionization does indeed occur in the LFS scrape-off layer of Alcator C-Mod [50], this 'main-chamber recycling' effect is primarily caused by a radial ion flux to wall surfaces – as required to satisfy *local* plasma/neutral mass balance. By this reasoning, such ionization-driven flows do not contribute to the global circulation loop that we are considered here. However, one must keep in mind that the *total* radial plasma flux at a given location on the LFS ($n\underline{V}_r$) must accommodate both a transport-driven poloidal circulation component ($nV_{tr,\theta}$) and any local ionization that arises from main-chamber recycling, $n\underline{V}_r = n\underline{V}_{tr,r} + n\underline{V}_{ion,r}$.

Adopting a simplified circular flux surface geometry, the divergence operator in the vicinity of the LCFS ($r \sim a$) can be approximated as

$$\nabla_r \cdot n\underline{V}_{tr,r} + \nabla_\theta \cdot n\underline{V}_{tr,\theta} \approx \frac{\partial}{\partial r} nV_{tr,r} + \frac{B_\theta}{a}\frac{\partial}{\partial \theta}\left[\frac{nV_{tr,\theta}}{B_\theta}\right] = 0 . \qquad (15)$$

Applying this to Eq. (14) and evaluating the result at the LFS midplane ($\theta = 0$) yields,

$$\left[\frac{\partial}{\partial r} nV_{tr,r}\right]_{LFS} = -B_{\theta,LFS}k(r) = -\frac{B_{\theta,LFS}}{a}\left[\frac{nV_{tr,\theta}}{B_\theta}\right]_{HFS} . \qquad (16)$$

Integrating Eq. (16) in minor radius yields the following expression,

$$nV_{tr,r}\Big|_{LFS} \approx \frac{B_{\theta,LFS}}{aB_{\theta,HFS}} \int_r^{r,\max} nV_{tr,\theta}\Big|_{HFS} dr \quad + nV_{tr,r}\Big|_{LFS,r-\max} . \qquad (17)$$

$nV_{tr,r}\big|_{LFS,r-\max}$ is the value of radial flux evaluated at a point in the far scrape-off layer ($r = r_{max}$). This non-zero quantity is needed since our measurements of $nV_{tr,\theta}/B_\theta$ on the HFS midplane do not extend all the way out to limiter/wall surfaces when mapped to the LFS midplane. Some estimate of $nV_{tr,r}\big|_{LFS,r-\max}$ is therefore required, as discussed below.

5.2 Comparison with fluctuation-induced radial flux measurements

Figure 13 shows the result of applying Eq. (17) to the symmetric (transport-driven) component of the boundary layer flow field (data shown in upper panels of Fig.7). The total poloidal flow velocity on the HFS is computed from the sum of parallel and $E_r \times B$ flow contributions (upper left panel). The poloidal flux density profile on the HFS ($nV_{tr,\theta}\big|_{HFS}$) is constructed using the density profile data (upper right panel). The radial flux density profile on the LFS midplane is computed from Eq. (17) and shown in the lower left panel. Since no HFS data exist for $\rho > 8$ mm, a value of $nV_{tr,r}$ at $\rho = 8$ mm must be specified ($=nV_{tr,r}\big|_{LFS,\rho=8\,mm}$). Three different cases are shown. The solid trace (case #2) chooses $nV_{tr,r}\big|_{LFS,\rho=8\,mm}$ so as to make $nV_{tr,r}$ linearly extrapolate to zero at the location of the LFS limiter. This is thought to represent the most plausible profile for $nV_{tr,r}$. Finally, radial velocity profiles ($V_{tr,r}$) corresponding to the three $nV_{tr,r}$ cases are assembled (red curves in lower right panel), using the measured LFS density profiles.

The lower right panel of Fig. 13 contains the key end result of this exercise – the consistency test. The blue curve is an independent measure of the radial transport velocity at the HFS midplane; it is the fluctuation-induced radial transport velocity ($V_r = \Gamma_r / n$), computed from the method outlined in section 2.3. The resultant Γ_r / n and $V_{tr,r}$ (case #2) profiles are found to be remarkably consistent, having similar same shapes and magnitudes. Thus it appears that we have assembled a consistent and complete picture of the transport-driven particle flow loops in Alcator C-Mod. The radial transport responsible for the transport-driven poloidal flow is identified as fluctuation-driven transport, localized near the LFS midplane. Perhaps a portion of the radial fluctuation-induced transport flux supports main-chamber recycling (i.e., V_r exceeds $V_{tr,r}$ in the far SOL), but a large fraction of it, particularly near the last-closed flux surface, is the 'transport' that drives the poloidal 'transport-driven flows' observed on the HFS midplane.

Having identified the particle source for the HFS poloidal flow, we next turn to the question of the sink mechanism, that is, how this flow terminates near the HFS divertor, and by what mechanism(s) the particles might be returning to the confined plasma region.

6. Poloidal Flow Particle Balance

One candidate mechanism for closing the particle circulation loop is neutral recycling from the HFS divertor region. If a sufficient fraction of the neutral flux produced at the inner divertor target is able to pass through the local SOL and ionize inside the separatrix or private flux regions, then poloidal flow particle balance might be explained. Another possible contributor is volume recombination. A region of detached plasma near the inner divertor strike point might send a sufficient flux of neutrals across the separatrix via this mechanism. Finally, there may be plasma transport mechanisms at play. Perhaps an inward particle pinch exists in the region between the HFS midplane and the inner divertor target, transporting ions from the HFS SOL directly into the core or the private flux regions.

In order to help address these questions, we quantify the magnitude of the poloidal flux circulating the plasma in the HFS scrape-off layer and compare it to the magnitude of the plasma flux at other poloidal locations, including the flux arriving at the inner divertor target. This is done for both favorable and unfavorable drift topologies. The influence of divertor recycling regimes (i.e., sheath-limited, high-recycling and partially detached) is also examined by tracking the poloidal fluxes as line-averaged plasma density is increased.

In short, we find that a robust poloidal circulation towards the inner divertor is maintained, independent of drift topology (favorable vs. unfavorable) and independent of the recycling regimes at the inner and outer divertors. The magnitude of the poloidal flow can be comparable to or can even exceed the total flux of ions arriving at the inner divertor target. These results indicate that the underlying flow closure mechanism does not simply involve equilibrium $E \times B$ drift flows in the divertor and x-point regions, since these change sign with B. Nor does it involve specific details of neutral recycling physics near the inner divertor target region. In this sense, the overall system behaves as if it is flux-driven: the magnitude of poloidal circulation is roughly fixed (apparently set by LFS radial transport) and is by necessity accommodated at the inner divertor plasma by perhaps a mixture of mechanisms. A special case is noted, however, in which a MARFE is observed in the boundary plasma. In this situation, the poloidal flow pattern on the HFS midplane is dramatically

altered. While this observation does not identify the mix of poloidal flow closure mechanism(s) in other regimes, it does show the potential impact that a volume-recombination zone can have on poloidal particle balance.

Finally, turning attention toward a possible turbulence-driven inward pinch mechanism, we examine fluctuation-induced particle fluxes measured in the HFS scrape-off layer. No evidence of an inward particle pinch is found in these data; the fluctuation-induced particle transport is essentially zero in this region. Thus, this part of the boundary layer flow story ends with an unsatisfying result; the underlying physics of the poloidal flow closure mechanism remains unresolved.

6.1 Poloidal Particle Flux, Γ_θ

The net poloidal particle flux, Γ_θ, at each scanning probe location can be readily computed from the measured parallel and perpendicular flow profiles (e.g., Fig. 5) combined with local density profile measurements. We define Γ_θ as the integration of the measured poloidal flux density through a toroidal area that is perpendicular to the flow direction and bounded by two flux surfaces,

$$\Gamma_\theta = \int_{r_1(\rho_1)}^{r_2(\rho_2)} n V_\theta 2\pi R dr, \qquad (18)$$

where $V_\theta = V_{ExB} B_\phi / B + V_{//} B_\theta / B$. The bounding flux surfaces, ρ_1 and ρ_2, are chosen to cover as much of the SOL as possible, while it must be restricted to the range where good data exist from all three scanning probes. The results shown in the following subsections were obtained by integrating the measured poloidal flux density over the first 7 mm of ρ-space (ρ_1 = 0 mm, ρ_2 = 7 mm). In real space, this covers about 7 mm at the horizontal probe location, 8.5 mm at the inner-wall scanning probe location and 10 mm at the vertical probe location.

It is important to point out that in this flux computation we do not include diamagnetic drifts. This is because we wish to compare Γ_θ flowing in the SOL to that arriving at divertor surfaces. While diamagnetic drifts do indeed produce a fluid motion, the guiding centers of the contributing particle orbits do not move; the particles simply gyrate in place; it is the spatial variation of their number densities and energies that contribute to diamagnetic fluid flow. Thus, the diamagnetic drift component of the flow field is divergence-free and self-terminating (apart from

toroidal effects that produce Pfirsch-Schlüter flows), especially at the divertor target interface. A more detailed discussion of this physics can be found in Chankin and Stangeby [51], in the context of identifying the appropriate fluid/surface boundary conditions at wall surfaces.

6.2 Variation of Γ_θ with Magnetic x-point Balance

The first question we address is whether Γ_θ, as computed from Eq. (18), is consistent with the poloidal flow picture that has been developed previously from parallel flow measurements alone [2] – a persistent flow on the HFS towards the active divertor, regardless of favorable vs. unfavorable $B\times\nabla B$ drift topology. It is appropriate that we revisit this question with our more complete flow data set, since due to the small magnetic field line angle on the HFS scrape-off layer, even a small $E_r\times B$ component may impact the net poloidal flow pattern.

As has been done in the past, we compare flow measurements from a series of otherwise identical discharges in which the magnetic x-point balance is systematically changed from lower single-null dominant (LSN) to upper single-null (USN) dominant. Figure 14 shows the result of applying Eq. (18) to data from all three scanning Langmuir-Mach probes. The horizontal axis corresponds to the distance between the primary and secondary separatrix locations, mapped to the outer midplane. Values less than zero correspond to LSN, near zero double-null (DN) and greater than zero USN. The vertical axis is poloidal flux in the electron diamagnetic drift direction. All discharges had normal current (0.8 MA) and field (5.4 tesla) directions. The data set includes a large number of discharges with a wide range of line-averaged plasma densities, $0.8 < \bar{n}_e < 1.8\text{x}10^{20}$ m^{-3}. The data are binned according to secondary separatrix position, with error bars indicating plus and minus one standard deviation about the mean value.

The well-established picture of HFS poloidal particle flux due to parallel flows is clearly reproduced in the upper panel of Fig. 14. Particle flux at the inner-wall probe location (HFS) is persistently directed toward the active divertor, i.e., toward the lower divertor for LSN and toward the upper divertor for USN. A nearly zero flow is seen under DN conditions. These data are also consistent with plasma flow observations from impurity 'plume' dispersal experiments at the inner wall midplane [52]. The full magnitude of the directed flow occurs when the relative separatrix locations are displaced by more than ~5 mm from DN. When $E_r\times B$ flow components are included, the net poloidal flux on the HFS is largely unchanged. Thus, our interpretation of the HFS particle flux picture is identical to that which was derived from parallel flow measurements alone and from

impurity plume dispersal; the net poloidal particle flux on the HFS is unambiguously directed toward the active divertor, in agreement with the transport-driven flow hypothesis.

Consistent with the analysis in section 3, the parallel and $E_r \times B$ flows are opposed in the LFS scrape-off layer, leading to a net poloidal flux that is small at the horizontal and vertical scanning probe locations. At the outer midplane (horizontal probe), both the parallel and the $E_r \times B$ flow components tend to become weaker in USN compared with LSN while nearly cancelling each other in either case. This observation tracks the overall trend seen directly in the data of Fig. 6; a stronger co-current toroidal rotation of the boundary plasma is seen under the conditions of favorable $B \times \nabla B$ drift direction. Its underlying cause can be traced to the transport-driven component of the boundary layer flow (section 3), shown in Fig. 8.

6.3 Variation of Γ_θ with Poloidal Location

The next question to address is the relative magnitude of Γ_θ flowing in the HFS scrape-off layer compared to Γ_θ arriving on the inner divertor and at other points in the SOL. To this end, a composite of all the probe-inferred Γ_θ measurements is assembled in Fig. 15. Here Γ_θ is shown as a function of normalized distance along a magnetic field line that starts on the outer divertor ($S = 0$) and ends on the inner divertor ($S = 1$). The total particle flux arriving at a divertor surface is simply computed from the ion saturation current density profile (measured by embedded probe arrays shown in Fig. 2), integrated over the same portion of flux space that is sampled by the scanning probes. Straight lines are drawn between measurement points to guide the eye. Up to five points are linked together, corresponding to the inner/outer divertor probes and the three scanning probes. The average values shown are obtained from a number of similar plasmas, binned and color-coded according to line-averaged density. The data shown in the upper panels of Fig. 15 are of primary interest (normal field and current direction, LSN/USN), since it includes measurements from all five probe systems. The data in the lower panels (reversed field and current direction, LSN/USN) are sparse, lacking good measurements from the inner-wall and vertical probes. Nevertheless, these data indicate that the reversed field data are roughly equivalent to forward field, swapping LSN for USN.

Comparing the configurations, one sees a clear asymmetry in the poloidal distribution of Γ_θ that depends on favorable vs. unfavorable $B\times\nabla B$ drift. For favorable $B\times\nabla B$ (upper-left and lower-right panels), Γ_θ is directed towards the inner divertor for all locations other than the outer divertor. For unfavorable $B\times\nabla B$ direction (lower-left and upper-right panels), the stagnation point in Γ_θ is located more towards the 'crown' of the plasma (i.e., the portion of the last-closed flux surface that is diametrically opposed to the x-point region). This behavior can be understood by looking at the contributions of the symmetric (transport-driven) and anti-symmetric (drift-driven) flow components on the LFS, derived in section 3. Figure 7 shows that the transport-driven poloidal flow is very small on the LFS; the drift-driven flows dominate there. On the other hand, Figs. 7 and 10 show that the drift-driven poloidal flows are composed of parallel ion Pfirsch-Schlüter flows in the electron diamagnetic direction, and perpendicular $E_r\times B$ flows in the ion diamagnetic direction. Since the ion Pfirsch-Schlüter flow is somewhat larger, a non-zero value of Γ_θ is seen at the LFS midplane, pointed in the electron diamagnetic direction. Thus, the stagnation point in Γ_θ tends to be shifted in the electron diamagnetic direction away from the LFS midplane, i.e., toward the 'crown' for unfavorable drift direction and toward the x-point for favorable drift. Note that this shift does not arise from the ballooning-like radial particle loss; on the basis of the measured transport-driven flow component, that loss appears to be centered roughly at the LFS midplane, regardless of magnetic topology.

6.4 Variation of Γ_θ with Plasma Density

Turning attention to the outer divertor fluxes (S = 0), we see an expected behavior. Significantly higher Γ_θ are recorded on the outer divertor surface than locations 'upstream' at the horizontal probe (HP) and vertical probe (VP) locations. This is consistent with the outer divertor operating as a 'high-recycling divertor,' meaning that most of the neutrals produced at the surface are re-ionized locally and return as ions to the divertor. As the line-averaged plasma density is increased, the particle flux to the outer divertor increases and the recycling flux is amplified. Yet, at the inner divertor we see a different behavior. In most cases, Γ_θ recorded at the inner divertor surface is a factor of two or less times the Γ_θ recorded at the inner-wall probe location (IWP). This is observed over the full range densities and in both topologies. Clearly, a different particle balance picture is required to explain these observations.

As the line-averaged density is increased in USN with normal field direction, the inner divertor Γ_θ goes from being ~2 times Γ_θ at the inner-wall location (IWP) to a value that is *less* than Γ_θ recorded at the IWP (see upper right panel in Fig. 15). This suggests that the inner divertor is entering a detached state at moderate densities while the outer divertor remains attached. Figure 16 examines these trends in more detail, tracing out Γ_θ at each measurement location as a function of line-averaged density. Focusing on the forward field/current data (top panel), we see that the inner and outer divertors do indeed have different behaviors. The outer divertor particle flux increases steadily with density in LSN, while the inner divertor shows almost no change. In USN, the outer divertor shows even higher flux at moderate densities, but begins to decrease at $\bar{n}_e \sim 1.4 \times 10^{20}$ m^{-3}. The inner divertor also shows an increase in flux with density, up to $\bar{n}_e \sim 1.25 \times 10^{20}$ m^{-3} at which point it begins to decrease as well, likely due to the onset of detachment at the inner divertor. The inner divertor flux is almost eliminated at a line-averaged density of 1.6×10^{20} m^{-3}. Yet, the fluxes recorded by the scanning probes and, most noteworthy the inner-wall scanning probe, show remarkably little sensitivity to line-averaged density.

Perhaps at high line-averaged densities, volume recombination is partially responsible for absorbing Γ_θ from the HFS and re-injecting a large fraction of it into the confined plasma as neutrals. Yet, this mechanism cannot be active at the lowest densities where the divertor is clearly attached – a point that is examined further in the next section. Thus, these data suggest that multiple mechanisms may act to close the HFS particle flux loop, with the dominant mechanism changing according to plasma density and magnetic topology.

Focusing on the reversed field data set (lower panel in Fig. 16), we see similarities between USN (LSN) discharges and LSN (USN) discharges in forward field. As expected from symmetry, the largest values of divertor particle flux under reversed field/current conditions are attained in LSN compared USN. However, an identical match between LSN-reversed field and USN-forward field cases is clearly not observed. For example, we do not see a roll-off in poloidal particle flux for LSN-reversed at high density, as observed for USN-forward field. Instead, Γ_θ increases monotonically up to the maximum densities measured ($\bar{n}_e = 1.6 \times 10^{20}$ m^{-3}). This result may be due to the different geometries in upper and lower divertors, which may affect the threshold conditions for divertor detachment.

6.5 Inner Divertor Conditions – Recycling and Volume Recombination Effects?

Electron temperature and pressure profiles measured at the inner divertor and inner wall locations are compared in Fig. 17 with the idea of looking for evidence of detachment physics contributing to poloidal particle balance, e.g., volume recombination and subsequent neutral transport into the confined plasma zone. These profiles correspond to the data points marked with circles in Fig. 16. Conditions at moderate line-averaged density ($\bar{n}_e \sim 1.1 \times 10^{20}$ m^{-3}) are shown in the left panels and high density ($\bar{n}_e \sim 1.6 \times 10^{20}$ m^{-3}) in the right panels.

For the USN cases (upper panels), we see that the inner divertor is in a high-recycling regime for the moderate density case: electron pressures map from the inner wall to the inner divertor probes, but with reduced electron temperature at the divertor. This may be consistent with the observation that Γ_θ at the inner divertor exceeds Γ_θ at the inner wall by about a factor of ~3 (see Fig. 16). For the high-density case, the inner divertor is clearly detached; divertor temperatures are below 5 eV through most of the SOL. This indicates that a significant amount volume recombination is present. The roll-over in the inner divertor Γ_θ with increasing line-averaged density seen in Fig. 16 is apparently a consequence of this physics. Therefore, it may be possible that the some of the HFS Γ_θ is converted to neutrals and redirected into the confined plasma by this mechanism.

Turning to the LSN cases (bottom panels), we see a markedly different picture. The inner divertor maintains a high-recycling state in both high and low density cases, with electron temperatures hovering slightly above the 5 eV level. If anything, the divertor becomes partially detached at high density for $\rho < 3$ mm, but the effect is not nearly as strong as that observed for the USN case at high density. Over the full range of densities, Γ_θ at the inner wall is comparable to Γ_θ at the inner divertor. In this respect, divertor recycling and detachment physics alone is not sufficient to account for the magnitudes of Γ_θ observed at the inner-wall and inner divertor locations.

Order-of-magnitude estimates of neutral penetration probabilities in the LSN inner divertor support a similar conclusion [30] – neutral transport and ionization physics by itself cannot account for the observed values of Γ_θ. Using a 1-D kinetic neutral transport code (KN1D [53]), neutrals were launched towards the last-closed flux surface (LCFS) at a starting flux surface location of ρ =5 mm and ρ =2 mm in the LSN inner divertor (moderate density, attached divertor case, shown in

Fig. 17). Measured densities and temperatures were specified as the plasma background conditions. The neutrals were found to have a probability of reaching the LCFS of only 14% and 25% respectively. Thus, in order to accommodate Γ_θ at the inner wall, Γ_θ at the inner divertor would have to be a factor of 4 to 7 larger, which is clearly not observed in these experiments.

6.6 Effect of MARFE on HFS profiles and flows

A MARFE [54, 55] is a plasma recombination zone occurring far away from divertor/limiter plasma contact regions: near a divertor x-point region (x-point MARFE), in the HFS scrape-off layer, or residing in vicinity of a secondary x-point zone (secondary x-point MARFE). This phenomenon occurs at high plasma densities where regions of the plasma periphery become cold enough to support it (< ~5eV). MARFEs are perhaps the most extreme example of volume recombination; in some situations they can dramatically reduce the plasma density on the HFS midplane and to change the observed HFS flow field. For this reason, they were mostly avoided in this experimental investigation. Yet, it is instructive to examine the impact that MARFEs have on the SOL, since it reveals the potential influence that a volume-recombination zone may have in affecting SOL particle balance.

Figure 18 shows two examples of similar plasmas (USN forward field – top panels, LSN reversed field – bottom panels) with and without the presence of secondary x-point MARFEs. The left panels show wide-format camera views of high-density C-Mod plasmas without MARFEs. In these cases, bright recycling light zones are seen localized to the inner divertor regions. The right panels are camera views of similar discharges at slightly higher density. Here, secondary x-point MARFEs appear in the camera images – bright zones located opposite to the 'active' divertor (i.e., at the bottom of the plasma for a USN discharge, top for USN). It is found on C-Mod that secondary x-point MARFEs occur at a slightly lower plasma density in the unfavorable $B\times\nabla B$ drift direction than in the favorable direction. Corresponding profiles of parallel Mach number and plasma electron pressure at different probe locations are shown below the camera images.

In the cases where the MARFE is present, the plasma electron pressure essentially disappears on the HFS SOL, as recorded by the inner wall (IWP) and inner divertor (IDIV) probes. In addition, the usual rapid plasma flow at the inner wall location (normally directed towards the inner divertor) is halted, and in what little plasma remains, flows in the *opposite direction*, i.e., towards the MARFE. Thus the MARFE acts as a very efficient particle sink – fully able to absorb

the incident Γ_θ generated via radial transport the LFS scrape-off layer and, apparently, sending this full flux of particles back into the confined plasma. The mechanism(s) by which these particles are returned to the confined plasma is not known, however. One possibility is that large temperature and density gradients associated with the MARFE lead to poloidal and radial $E \times B$ drifts, mixing the plasma across the last-closed flux surface. Another possibility is that the MARFE is able to inject a substantial neutral flux into the confined plasma from its volume recombination source. Perhaps the close proximity of this region to the last-closed flux surface enables the latter mechanism. In any case, these observations support the overall hypothesis that a detached inner divertor could, at least in part, close the poloidal flow loop by similar mechanisms – although we do not yet have the diagnostics in place to investigate these directly.

6.7 Inward particle pinch on HFS midplane?

Consistent with our direct measurements of Γ_θ and simple neutral mean-free-path considerations, many edge simulations have found neutral penetration to be insufficient to 'close the loop' on the observed HFS plasma flow pattern [25, 26] and impurity deposition patterns [27, 28]. The authors of these studies have suggested that an inward particle pinch might play a role in the HFS scrape-off layer, pulling ions back into the confined plasma. The required inward radial velocity is estimated to be in the range of 10-30 m/s (see Table 2).

Table 2: Magnitude of HFS pinch velocity required to close the observed HFS flow loop.

Author	**Tokamak**	**Modeling Code**	**Pinch Velocity**
Pigarov [26]	Alcator C-Mod	UEDGE	> 20 m/s
Elder [28]	DIII-D	OEDGE	10-30 m/s
Kirnev [25]	JET	EDGE2D	10 m/s

Referring to the measurements of Γ_θ in Fig. 16, we see that a typical value of Γ_θ in the HFS SOL is $\sim 2 \times 10^{21}$ s^{-1}. Based on the area of the last closed flux surface on the HFS (~ 2 m^2) and the plasma density there ($\sim 10^{20}$ m^{-3}), an inward pinch on the order of ~10 m/s acting over the entire HFS SOL could solve the particle balance puzzle. Note that a static Γ_r driven by poloidal electric

fields in the SOL not plausible; static E_θ would have to be on the order of 80 volts/m in C-Mod, corresponding to a potential variation along field lines of ~60 volts from the crown to the divertor x-point. For this reason it is thought that an inward pinch, if it exists, might arise from fluctuation-induced particle transport – something that can be readily examined using C-Mod's inner-wall scanning probe.

Fluctuation-induced radial transport velocities, $V_r = \Gamma_r / n$, from all three scanning probe systems are shown in Fig. 19 (see section 2.3 for method). The profiles in the top panel are obtained from averaging all available data, regardless of conditions – 85 probe scans, including a range of line-averaged densities in LSN and USN. All discharges had forward field (5.4 T) and current (0.8 MA). These data show quite a dramatic result: while horizontal and vertical probes display their typical V_r values of 50 to 100 m/s, the inner-wall probe reports essentially *zero fluctuation-induced transport*. Values of Γ_r / n_e from individual scans at the location of ρ = 1 mm are shown in the lower panel, sorted according to line-averaged density. While there is significant scatter in these data, the trends are robust; the data do not depend on digital sample rate or line averaged density. Profiles of Γ_r / n_e from individual inner-wall probe scans are examined in detail in Fig. 20. Again, there is significant scatter in the data, but no evidence of a non-zero averaged value of Γ_r / n_e, outside the statistical error bars. Thus we can confidently conclude that, not only is there no evidence of an inward particle pinch effect on the HFS midplane, the fluctuation-induced radial transport velocity at this location is essentially zero: V_r = 0 ±2 m/s. Apparently, the SOL plasma exhibits the maximum possible poloidal asymmetry in fluctuation-induced particle transport; all particles that leave the confined plasma via turbulence do so through LFS scrape-off layer only.

It is instructive to look at the fluctuating density and electric field components that give rise to the difference in transport on the LFS and HFS SOLs. Figure 21 shows representative fluctuation time series data sampled near the LFS and HFS midplanes. These are normalized ion saturation currents (from NE and SE electrodes) and radial $E \times B$ velocities computed from the differences in floating potentials from the NW and SW electrodes (see Fig. 4). The amplitudes of density (~Isat) and electric field fluctuations are greatly reduced and shifted to lower frequencies on the HFS. In addition, the two components are weakly correlated. These effects combine to produce essentially zero time-averaged fluctuation-induced radial transport fluxes at the HFS midplane.

In summary, we conclude that there is no evidence of a turbulent particle pinch at the HFS midplane of Alcator C-Mod. While we cannot rule out a pinch that might be highly localized

around the X-point, or a pinch that may arise from quasi-static convective cells localized to the X-point or divertor region (associated with an x-point MARFE, for example), our data shows no evidence of any fluctuation-induced particle flux crossing the LCFS near the HFS midplane.

7. Poloidal Heat Flow in HFS Scrape-off Layer

Finally, we turn to the topic of poloidal heat convection in the high-field side scrape-off layer and its impact on heat flow to the inner divertor target plate. Probe measurements at the LFS midplane, HFS midplane and inner divertor are used to quantify the relative importance of heat convection (parallel and perpendicular) compared to heat conduction. It is found that the parallel heat convection in the HFS scrape-off layer (arising from transport-driven flow) plays a dominant role, particularly in the far SOL where T_e is low and parallel conduction is relatively ineffective. $E_r \times B$ flow (drift-driven flow) also plays a key role, being of similar magnitude to the poloidal projection of parallel heat conduction. At low plasma densities, the drift-driven component *opposes* heat transport to the inner divertor in favorable topologies and *reinforces* heat transport to the inner divertor in unfavorable topologies. This mechanism, amplified by divertor radiation and recycling, is a leading candidate to explain inside-outside divertor asymmetries that depend on $\boldsymbol{B} \times \nabla B$ drift direction. It also is found to play a role in explaining a puzzling observation that was initially made with C-Mod's inner-wall scanning probe: a low-T_e plasma state in the HFS scrape-off layer at low plasma densities when inner divertor is *attached* – conditions that are normally expected to favor high T_e in the HFS SOL. These observations underscore the complicated interplay that can occur among SOL plasma flows, heat transport and divertor asymmetries.

7. 1 Poloidal Heat Flux Computation

Parallel conduction, parallel convection and perpendicular convection are the dominant contributors to poloidal heat flow along a flux surface in a scrape-off layer. Under the assumptions that $T_i = T_e$ and $n_i = n_e$, a fluid representation [56] for parallel heat flux, including both conductive and convective terms is

$$q_{\parallel} = q_{conv} + q_{cond} = 5nkT_e V_{\parallel} - \kappa_{\parallel}^{e} \nabla_{\parallel} T_e . \qquad (19)$$

For the case of a deuterium plasma, this can be evaluated as

$$q_{\parallel} = 770 n_{20} M_{\parallel} T_e^{3/2} - 52 \nabla_{\parallel} T_e^{7/2} \quad [\text{kW m}^{-2}] \tag{20}$$

with T_e in units of eV and n_{20} in 10^{20} m^{-3}. The temperature-dependence of $\kappa_{\parallel}^{e}$ produces a parallel conduction component that scales with the parallel gradient of $T_e^{7/2}$. Projecting this heat flux in the poloidal direction and adding perpendicular convection from $E_r \times B$ drifts, yields an expression for the local poloidal heat flux density,

$$q_{\theta} = (770 n_{20} M_{\parallel} T_e^{3/2} - 52 \nabla_{\parallel} T_e^{7/2}) \frac{B_{\theta}}{B} + 0.08 n_{20} T_e V_{ExB} \frac{B_{\phi}}{B} \quad [\text{kW m}^{-2}] . \tag{21}$$

Classical perpendicular conduction is negligible compared to parallel conduction, even accounting for small field line angles. Diamagnetic heat flow components (conduction and convection) are also not included because, in addition to the usual argument that these flows are nearly divergence-free and self-terminating, the ion and electron contributions are equal and opposite when $T_i = T_e$.

With the exception of the $\nabla_{\parallel} T_e^{7/2}$ term, all quantities in Eq. (21) can be readily evaluated at the location of the inner-wall scanning probe, which measures directly n_{20}, $M_{\parallel}$, T_e, and V_{ExB}. In order to quantify $\nabla_{\parallel} T_e^{7/2}$, a simplified model of scrape-off layer heat flow is used, which assumes that all heat enters the SOL via ballooning-like transport near the LFS midplane (see Fig. 22). In the situation in which parallel conduction is the sole contributor to heat flow along field lines, $q_{\parallel}$ is simply proportional to $\nabla_{\parallel} T_e^{7/2}$. Thus, $T_e^{7/2}$ varies linearly with parallel distance in regions where $q_{\parallel}$ is constant. We therefore use a simple fitting technique to estimate $\nabla_{\parallel} T_e^{7/2}$ at the inner-wall scanning probe location: straight lines are drawn between probe measurements of $T_e^{7/2}$ at the horizontal, inner-wall and inner divertor probe locations when plotted versus distance along field lines. The local value of $\nabla_{\parallel} T_e^{7/2}$ is taken to be the average slope of these two lines.

7. 2 Poloidal Heat Flux Components in the HFS SOL

Figure 23 shows the result of applying the above procedure to extract cross-field profiles of the three dominant components to the poloidal heat flux at the inner-wall midplane location: parallel conduction, parallel convection and perpendicular convection. The data shown are average values from multiple discharges with forward toroidal field (5.4T) and plasma current (0.8 MA). Data are separated into those obtained from low ($0.7 \times 10^{20} < \bar{n}_e < 1.0 \times 10^{20}$ m^{-3}) and moderate ($1.0 \times 10^{20} < \bar{n}_e < 1.6 \times 10^{20}$ m^{-3}) line-averaged density discharges and from lower-single null and upper-

single null discharges. Error bars indicate plus and minus one standard deviation in the computed mean value.

Several important observations can be made from Fig. 23:

1. Parallel heat convection (arising from the transport-driven plasma flow component) is clearly the dominant poloidal heat transfer mechanism in the HFS SOL under all the discharge conditions that were investigated.
2. Perpendicular heat convection has a tendency to reverse direction from LSN to USN, as expected for drift-driven flow. At low density, the heat flow in a radial zone that spans the region 2 mm < ρ < 5 mm is directed away from the inner divertor in LSN (unfavorable $B \times \nabla B$ direction) and toward the inner divertor in USN.
3. At high density, the perpendicular convection tends to reverse with topology, but in the opposite way. In particular, $E_r \times B$ heat convection in the near SOL (ρ < 2 mm) is directed toward the inner divertor in LSN and away from the inner divertor in USN. This drift-driven heat flow pattern is the result of radial electric fields that point *inward* in minor radius rather than outward – a feature that is normally characteristic of closed field line regions.
4. At high density, parallel heat convection is larger in the far SOL (ρ > 6 mm) for LSN compared to USN discharges. In addition, the heat conduction term is larger in the near SOL for LSN compared to USN discharges. These two effects, combined with the behavior of $E_r \times B$ heat convection discussed in (3) above, lead to higher poloidal heat flux toward the divertor in LSN compared to USN at high plasma densities.

Observation (2) offers an explanation for a result obtained with the inner-wall scanning probe what was initially quite puzzling: low electron temperatures in LSN discharges at low density when the inner divertor is clearly attached. Furthermore, the electron temperature there was seen to *increase* as the plasma density is raised. These observations are illustrated in Fig. 24. When the line-averaged density enters the range $0.8 \times 10^{20} < \bar{n}_e < 1.1 \times 10^{20}$ m^{-3}, T_e at the inner-wall scanning probe location drops markedly and the floating potential increases. The temperature reduction is most pronounced at the radial location shown in the figure ($\rho \sim 4$ mm). The increase in floating potential is consistent with the drop in electron temperature and the requirement that plasma

potential ($\sim V_f + 2.7T_e$) be similar to that observed by other scanning probes on the same flux surface. The source of the phenomenon is apparently due to $E_r \times B$ heat convection. Under the same conditions that favor the low T_e condition, $E_r \times B$ heat convection opposes the poloidal heat flow from the LFS scrape-off layer to HFS scrape-off layer.

These overall observations are consistent with those reported by Hutchinson *et al*. [10, 32], in which field reversal was used rather than topology reversal to change the direction of $\boldsymbol{B} \times \nabla B$ with respect to the x-point. Lower T_e values were observed in the inner divertor with favorable drift direction compared to unfavorable drift direction. It was argued that the asymmetry was more likely the result of a heat flux asymmetry than a pressure asymmetry. $E_r \times B$ heat convection was proposed as the cause for the observed asymmetry, consistent with the direct measurements presented here.

Hutchinson *et al*. also observed that divertor heat flux asymmetries between favorable and unfavorable drift directions are greatly reduced at high density, as are radiation asymmetries from the divertor legs. This is consistent with our observations as well. For densities above $\bar{n}_e \sim 1.0 \times 10^{20}$ m^{-3}, $E_r \times B$ heat convection becomes a smaller contributor to the total heat flux in much of the HFS scrape-off layer ($\rho > 2$ mm). Therefore, $\boldsymbol{B} \times \nabla B$ reversal does not influence the HFS SOL conditions at high density as much as it does at low density.

Finally, observations (3) and (4) above indicate that at high density, unfavorable $\boldsymbol{B} \times \nabla B$ discharges (USN in the case of Fig. 23) have reduced poloidal heat flux toward the inner divertor. This is consistent with the observation of a reduced density threshold for MARFE onset with unfavorable drift direction. When the poloidal heat flux toward the inner divertor is reduced, the HFS SOL can more easily reach temperatures low enough for volume recombination.

8. Summary and Conclusions

Utilizing the unique set of probe diagnostics available on Alcator C-Mod, including a scanning Langmuir-Mach probe on the high-field side (HFS) scrape-off layer (SOL), the underlying physics that leads to the complex pattern of boundary layer flows observed in tokamaks has been investigated in ohmic L-mode discharges with unprecedented detail. It is found that the plasma flow pattern can be decomposed into two principal parts: (1) a drift-driven component, which lies within a magnetic flux surface and is divergence-free and (2) a transport-driven

component, which gives rise to near-sonic parallel flows on the high-field side scrape-off layer. Toroidal rotation, Pfirsch-Schlüter and transport-driven contributions are unambiguously identified. The magnitude of the transport-driven flow component is found to be quantitatively consistent with radial fluctuation-induced particle fluxes measured on the low-field side, identifying this as the primary driver. Thus we have clearly identified the 'transport' that is responsible for the observed 'transport-driven parallel flows' in the HFS SOL. We also find a transport-driven flow on the low-field (LFS) scrape-off layer – a nearly perfect toroidal rotation that is co-current directed under favorable drift conditions and counter-current directed in unfavorable conditions. This flow response is consistent with the idea that transport-driven parallel flows impose a flow boundary condition at the last-closed flux surface [2]. Drift-driven and transport-driven components sum constructively for favorable drift direction and destructively for unfavorable drift direction, tending to produce larger (or smaller) poloidal flow velocities in favorable (or unfavorable) drift topologies. Such an effect may be important as it could influence the overall flux-gradient relationships via differences in equilibrium flow shear [1].

In stark contrast to the behavior on the LFS midplane, fluctuation-induced fluxes at the HFS midplane are measured to be essentially zero. This unique measurement clearly documents the extreme poloidal asymmetry in fluctuation-induced transport that is exhibited by a tokamak plasma – a phenomenon that drives much of the physics seen in the HFS SOL: plasma exists there because it flows freely along field lines from the LFS SOL. As a result, parallel flows are found to dominate both particle and heat transport in this region. The lack of fluctuation-induced transport also excludes the idea that an 'inward pinch' mechanism is occurring on the HFS midplane and that this mechanism plays a role in closing the overall particle flow loop. Instead, our measurements indicate that the flow loop must be closing in the vicinity of the inner divertor region. The poloidal projection of the particle flow is found to be remarkably large, corresponding to a factor of ~1/3 to ~1 times the total ion flux arriving on the inner divertor. Moreover, the magnitude of the flow is insensitive to inner divertor conditions, persisting at similar levels in sheath-limited, high-recycling and detached inner divertor conditions. These observations suggest that the flow-closure mechanism in the inner divertor region involves multiple mechanisms that could carry plasma into the confined plasma and/or private flux zone: neutral recycling, $E \times B$ flows, volume recombination, turbulent transport. In special cases when a secondary x-point MARFE is seen, flows on the HFS SOL are dramatically altered – evidence that volume recombination can have a strong influence on

the poloidal flow loop. In any case, the overall system behaves as if it is 'flux-driven'; the inner divertor region appears to accommodate whatever flux arrives from the transport-driven flow, a flow driven by the radial transport on the LFS SOL.

Taking advantage of the unique inner-wall scanning Langmuir-Mach probe system, plasma heat flow measurements in the HFS SOL are reported (parallel convection, parallel conduction and $E_r \times B$ heat convection). These data address the root causes of the inside-outside divertor asymmetries that have been observed previously in C-Mod and elsewhere. Parallel heat *convection* clearly dominates the overall poloidal flow of heat to the inner divertor, with parallel electron heat conduction and $E_r \times B$ heat convection playing subdominant roles with about equal magnitude. However, $E_r \times B$ heat convection reinforces or opposes heat flow to the inner divertor region, depending on the direction of $\boldsymbol{B} \times \nabla B$ relative to the x-point (which sets the direction of the toroidal field) and the plasma density (which affects the sign of E_r in the region near the last-closed flux surface). As a result, the behavior or $E_r \times B$ heat convection in the HFS SOL helps to explain the observations of strong inside-outside divertor asymmetries that favor low-T_e (high-T_e) in the inner divertor at low and moderate plasma densities for favorable (unfavorable) $\boldsymbol{B} \times \nabla B$ direction.

Acknowledgements

Alcator C-Mod's contributions to fusion energy science are made possible by the excellent engineers, technical staff, students, and scientists on the Alcator team. This work is supported by U.S. Department of Energy Coop. Agreement DE-FC02-99ER54512.

References

[1] LaBombard, B., et al., Phys. Plasmas 15 (2008) 056106.
[2] LaBombard, B., et al., Nucl. Fusion 44 (2004) 1047.
[3] Stangeby, P.C., J. Nucl. Mater. 415 (2011) S278.
[4] Wan, A.S., LaBombard, B., Lipschultz, B., and Yang, T.F., J. Nucl. Mater. 145-147 (1987) 191.
[5] Vershkov, V.A., Grashin, S.A., and Chankin, A.V., J. Nucl. Mater. 145 (1987) 611.
[6] Vershkov, V.A., J. Nucl. Mater. 162 (1989) 195.
[7] Pitts, R.A., Vayakis, G., Matthews, G.F., and Vershkov, V.A., J. Nucl. Mater. 176 (1990) 893.
[8] Boucher, C., MacLatchy, C.S., Le Clair, G., Lachambre, J.L., and St-Onge, M., J. Nucl. Mater. 176 (1990) 1050.
[9] MacLatchy, C.S., et al., J. Nucl. Mater. 196-198 (1992) 248.
[10] LaBombard, B., et al., J. Nucl. Mater. 241-243 (1997) 149.
[11] Boedo, J.A., et al., J. Nucl. Mater. 266 (1999) 783.
[12] Asakura, N., et al., IAEA. Nuclear Fusion 39 (1999) 1983.
[13] Asakura, N., et al., Phys. Rev. Lett. 84 (2000) 3093.
[14] Erents, S.K., Chankin, A.V., Matthews, G.F., and Stangeby, P.C., Plasma Phys. Control. Fusion 42 (2000) 905.
[15] Gunn, J.P., et al., Phys. Plasmas 8 (2001) 1995.
[16] Asakura, N., et al., J. Nucl. Mater. 313-316 (2003) 820.
[17] LaBombard, B., Gangadhara, S., Lipschultz, B., and Pitcher, C.S., J. Nucl. Mater. 313-316 (2003) 995.
[18] Asakura, N., et al., Nucl. Fusion 44 (2004) 503.
[19] Erents, S.K., Pitts, R.A., Fundamenski, W., Gunn, J.P., and Matthews, G.F., Plasma Phys. Control. Fusion 46 (2004) 1757.
[20] Smick, N., LaBombard, B., and Pitcher, C.S., J. Nucl. Mater. 337-339 (2005) 281.
[21] Gunn, J.P., et al., J. Nucl. Mater. 363-365 (2007) 484.
[22] Pitts, R.A., et al., J. Nucl. Mater. 363-365 (2007) 505.
[23] Asakura, N., J. Nucl. Mater. 363-365 (2007) 41.
[24] Fedorczak, N., Gunn, J.P., Ghendrih, P., Monier-Garbet, P., and Pocheau, A., J. Nucl. Mater. 390-391 (2009) 368.
[25] Kirnev, G.S., et al., J. Nucl. Mater. 337-339 (2005) 271.
[26] Pigarov, A.Y., Krasheninnikov, S.I., LaBombard, B., and Rognlien, T.D., Contributions to Plasma Physics 48 (2008) 82.
[27] Groth, M., et al., Phys. Plasmas 14 (2007) 056120.
[28] Elder, J.D., et al., J. Nucl. Mater. 390-391 (2009) 376.
[29] Chankin, A.V., et al., Nucl. Fusion (2007) 762.
[30] Smick, N., "Plasma Flows in the Alcator C-Mod Scrape-Off Layer", PhD Thesis (Cambridge: MIT) 2009, MIT PSFC Research Report: PSFC/RR-09-15, http://www.psfc.mit.edu/library1/catalog/restricted/rr_reports/09rr015/09rr015_full.pdf.
[31] Smick, N. and LaBombard, B., Rev. Sci. Instrum. 80 (2009) 023502.
[32] Hutchinson, I.H., et al., Plasma Phys. Contol. Fusion 37 (1995) 1389.
[33] Hutchinson, I.H., et al., Phys. Plasmas 1 (1994) 1511.
[34] Granetz, R.S., Hutchinson, I.H., Gerolamo, J., Pina, W., and Tsui, C., Rev. Sci. Instrum. 61 (1990) 2967.
[35] Lao, L.L., et al., Nucl. Fusion 25 (1985) 1611.
[36] MacLatchy, C.S., Boucher, C., Poirier, D.A., and Gunn, J., Rev. Sci. Instrum. 63 (1992) 3923.
[37] Hutchinson, I.H., Phys. Rev. Lett. 101 (2008) 035004.
[38] Hutchinson, I.H., Phys. Plasmas 15 (2008) 123503.

[39] Graf, A., May, M., and Beiersdorfer, P., Rev. Sci. Instrum. 79 (2008) 10.
[40] Hutchinson, I.H., Physical Review A 37 (1988) 4358.
[41] Stangeby, P.C., Phys. Fluids 27 (1984) 682.
[42] Langley, R.A., et al., Data compendium for plasma-surface interactions, Nuclear Fusion, Special Issue, IAEA, Vienna (1984).
[43] LaBombard, B., Phys. Plasmas 9 (2002) 1300.
[44] Pfirsch, D. and Schluter, A., The Influence of Electrical Conductivity on the Equilibrium Behaviour of Low Density Plasmas in Stellarators, Max Planck Institute for Physics and Astrophysics Research Report: MPI/PA/62, (1962),
[45] Catto, P.J., Phys. Plasmas 13 (2006) 052507.
[46] Catto, P.J., Phys. Plasmas 14 (2007) 029901.
[47] Helander, P. and Sigmar, D.J., Collisional Transport in Magnetized Plasmas (Cambridge University Press, 2005).
[48] McDermott, R.M., et al., Phys. Plasmas 16 (2009) 056103 (12 pp.).
[49] Brunner, D., et al., Bull. Amer. Phys. Soc. 57 (2012) 38.
[50] LaBombard, B., et al., Nucl. Fusion 40 (2000) 2041.
[51] Chankin, A.V. and Stangeby, P.C., Plasma Phys. Control. Fusion 36 (1994) 1485.
[52] Jablonski, D., et al., J. Nucl. Mater. 241-243 (1997) 782.
[53] LaBombard, B., KN1D: A 1-D Space, 2-D Velocity, Kinetic Transport Algorithm for Atomic and Molecular Hydrogen in an Ionizing Plasma, M.I.T. Plasma Science and Fusion Center report PSFC/RR-01-3 Research Report: PSFC/RR-01-3, http://www.psfc.mit.edu/library1/catalog/reports/2000/01rr/01rr003/01rr003_abs.html.
[54] Lipschultz, B., et al., Nucl. Fusion 24 (1984) 977.
[55] Lipschultz, B., et al., Phys. Rev. Lett. 81 (1998) 1007.
[56] Braginskii, S.I., in Reviews of Plasma Physics (1965) (Consultants Bureau, New York) 1, 205.

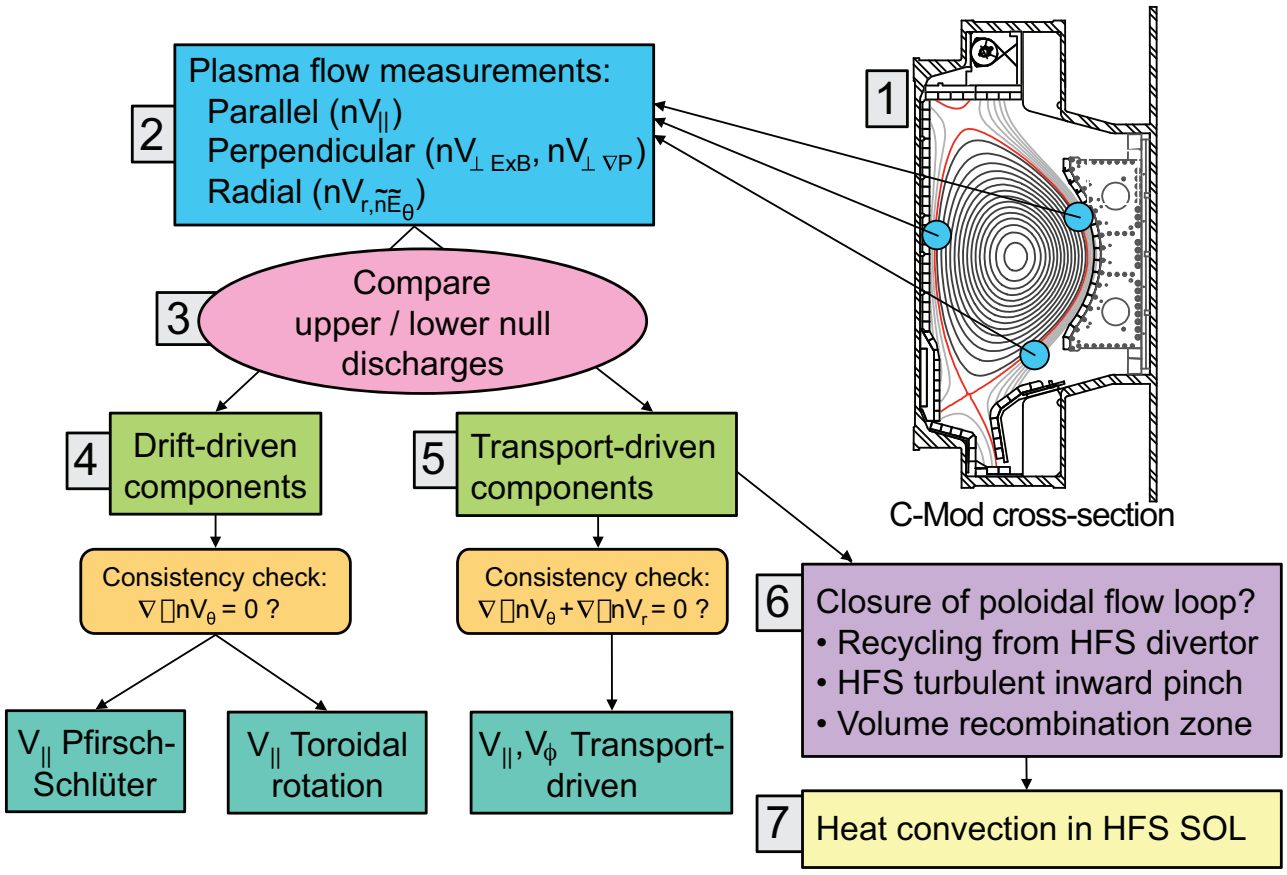

Figure 1. Experimental investigation of plasma flows reported in this paper. This graphic also serves as a table-of-contents, with section numbers indicated.

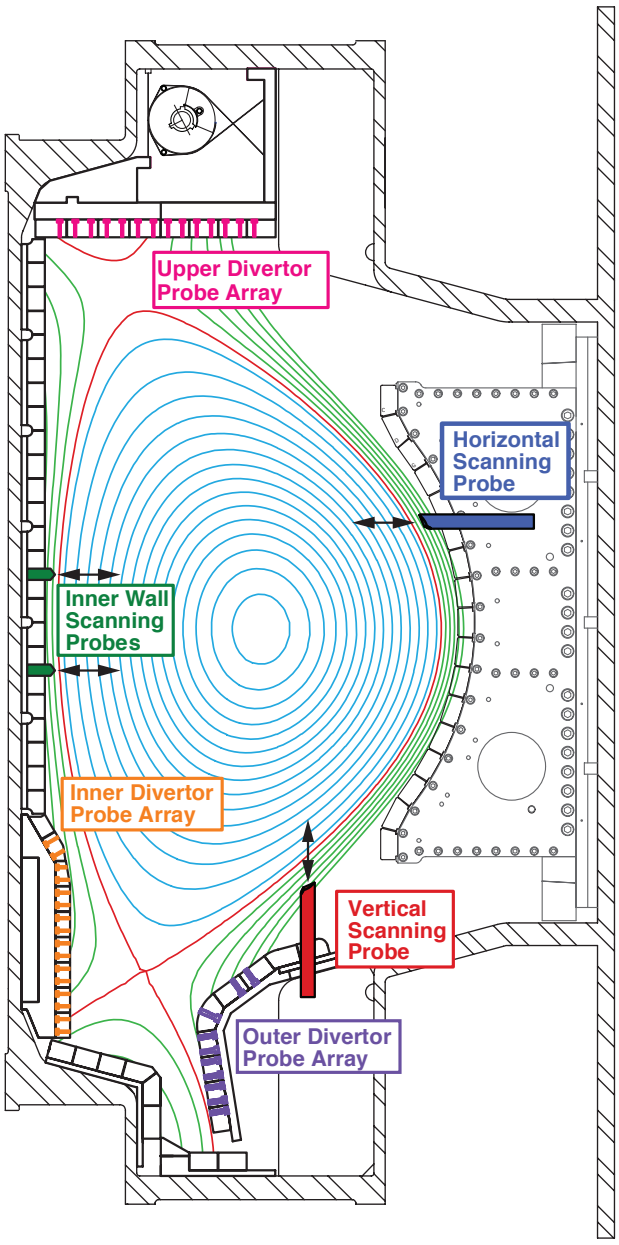

Figure 2. Cross-section of Alcator C-Mod showing locations of probes used in this study. Scanning Langmuir-Mach probes are located 10 cm above the outer midplane (Horizontal Scanning Probe), 39 cm below the outer midplane (Vertical Scanning Probe) and 5 cm below and above the inner midplane (Inner Wall Scanning Probes). These record profiles of plasma flows, plasma density, n, and electron temperature, T_e, in detail. Divertor conditions (incident ion fluxes, n, T_e) at the inner and outer leg locations in both lower-single null (LSN) and upper-single null (USN) discharges are recorded with Inner, Outer and Upper Divertor Probe Arrays. An example of a near double-null (DN) magnetic equilibrium is shown.

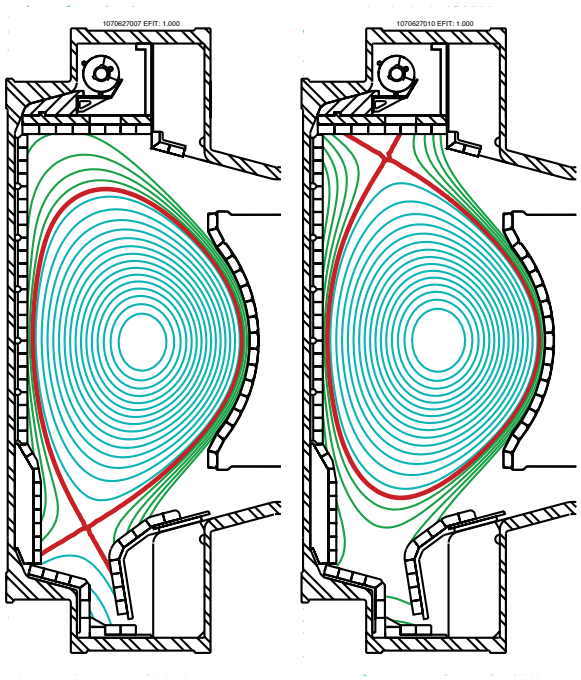

Figure 3. Examples of lower-single null (LSN - left) and upper single-null (USN - right) equilibria. Scrape-off layer profiles and flows are compared in otherwise matched discharges in which the last-closed flux surface (LCFS) is flipped symmetrically from LSN to USN. The influence of divertor geometry is assessed by performing LSN/USN comparisons with both forward and reversed magnetic field directions. In all cases, a right-handed helical magnetic field line topology is maintained, requiring plasma current and toroidal field direction to be changed together.

"Transport and drift-driven plasma flow components in the Alcator C-Mod boundary layer", N. Smick, B. LaBombard and I.H. Hutchinson

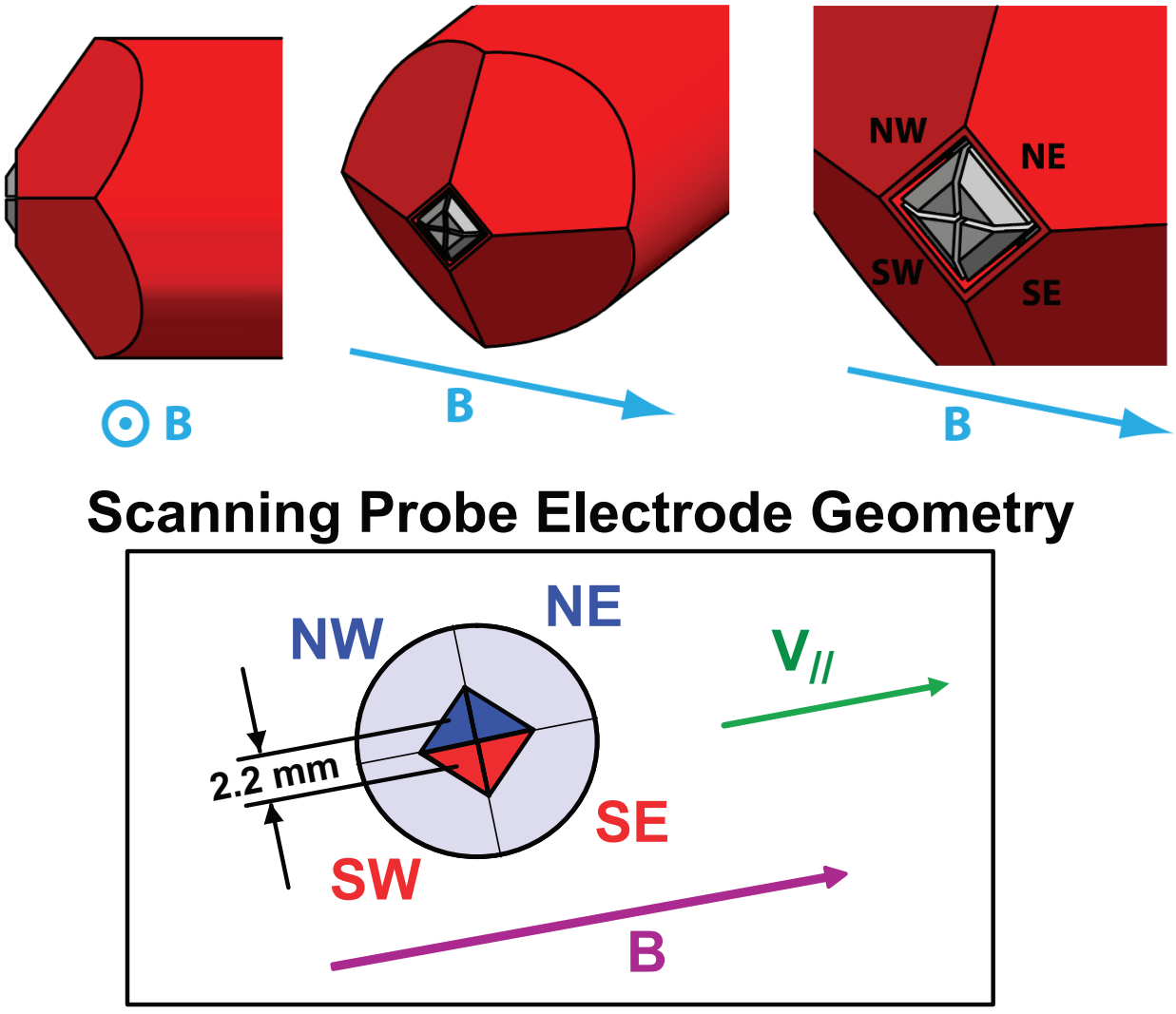

Figure 4. All scanning Langmuir-Mach probes use the same 4-electrode pyramidal geometry, which is aligned with respect to the local magnetic field direction. Plasma flow along the magnetic field is inferred by comparing ion saturation currents collected by 'east' (NE, SE) versus 'west' (NW, SW) electrodes. Radial fluctuation-induced particle fluxes are inferred by operating one 'north' (NW or NE) and one 'south' (SW or SE) electrode in a floating mode while recording ion saturation currents on the other two. Plasma density, potential and electron temperature are obtained by averaging data from all four electrodes.

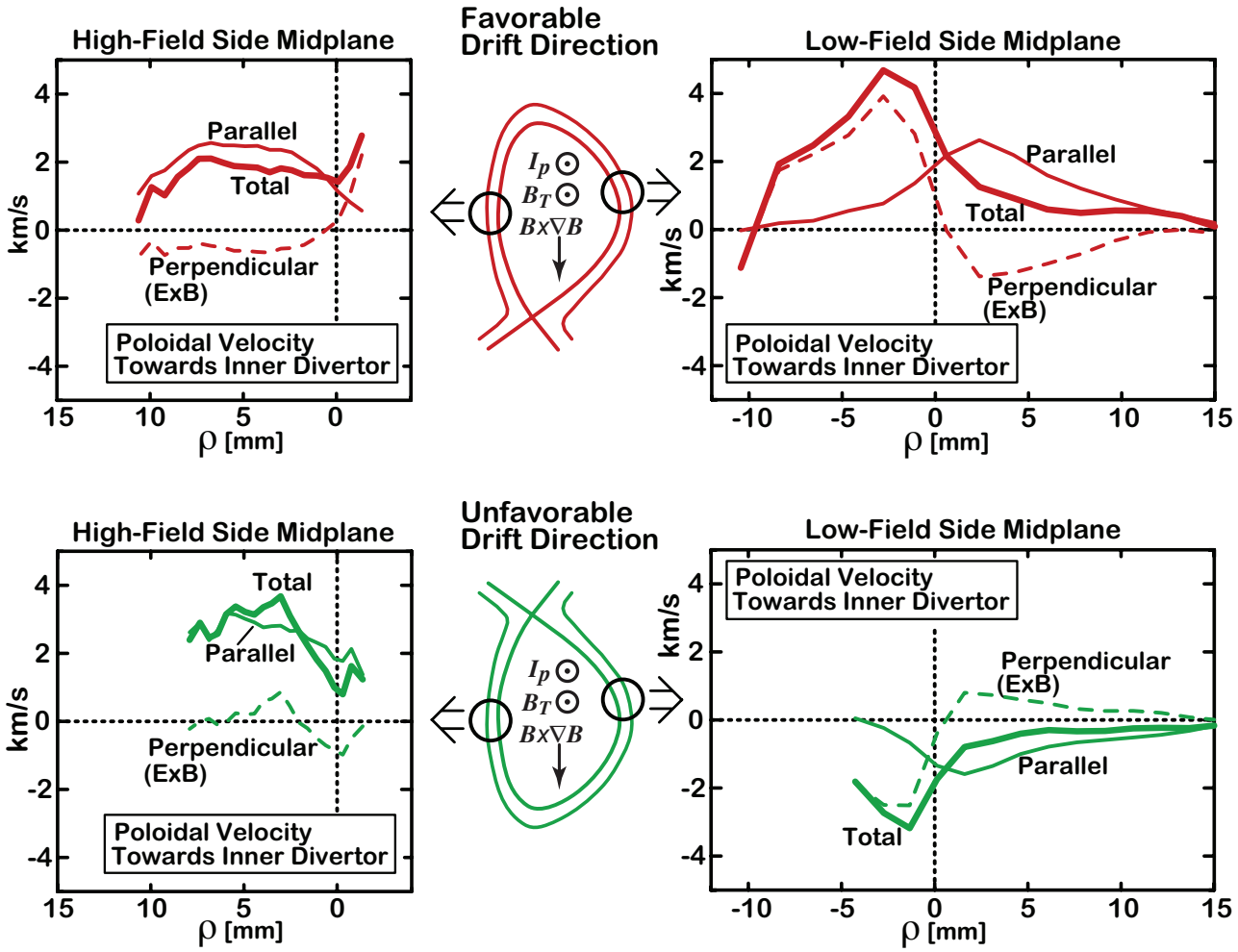

Figure 5. Poloidal projections of parallel and perpendicular ($E_r \times B$) flow velocities measured on the high-field side (HFS) and low-field side (LFS) midplane locations for forward and reversed field directions. Thick lines indicate the total poloidal flow velocity, which is the sum of parallel (thin line) and $E_r \times B$ (thin, dashed line) flow components, projected in the poloidal direction. Positive velocities indicate flow directed toward the inner divertor. Note the reversal of the ρ-axis in the left panels. The net poloidal flow on the HFS is largely determined by the parallel flow, which is always directed toward the inner divertor. The net poloidal flow on the LFS involves interplay between parallel and $E_r \times B$ flows.

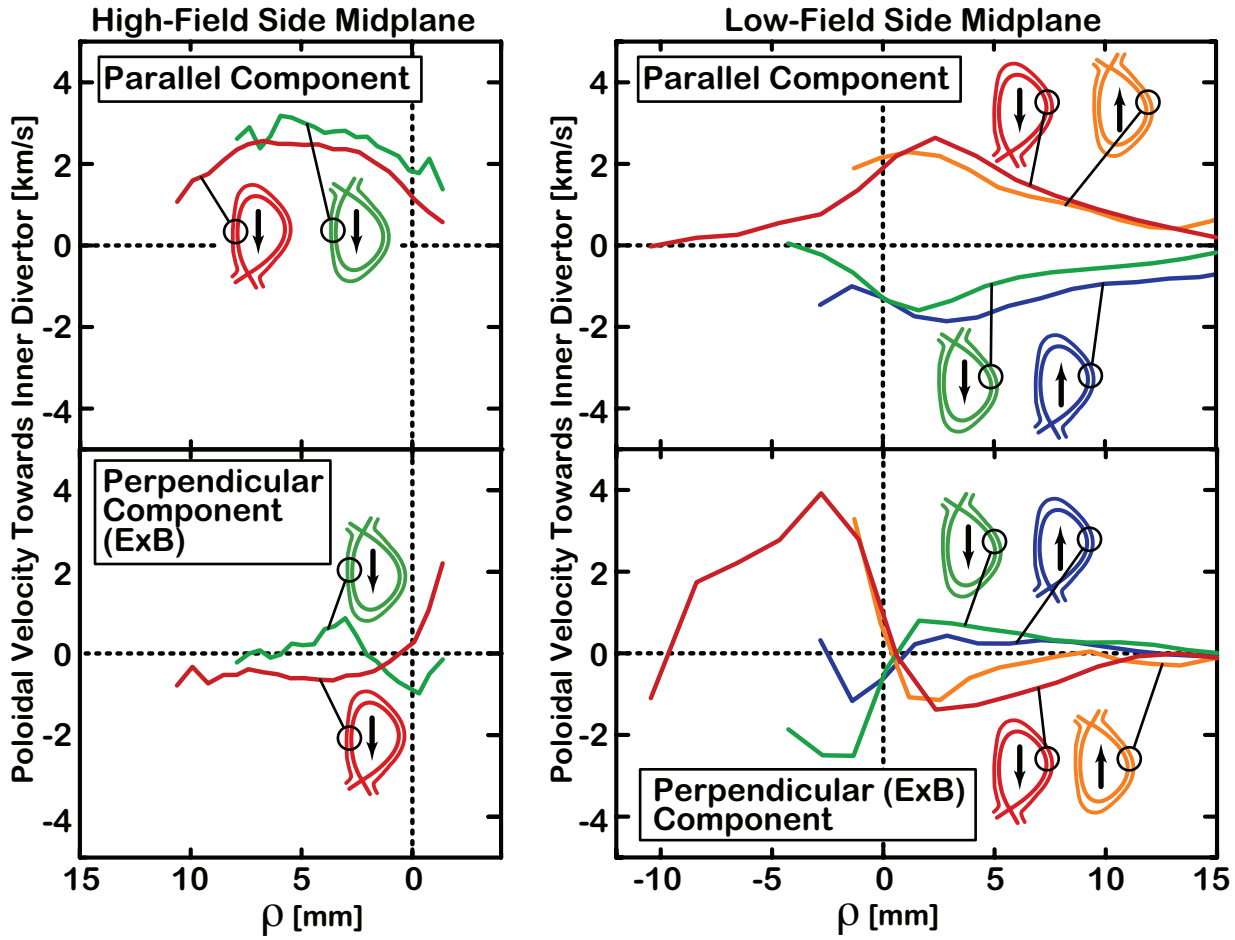

Figure 6. Same data as in Fig. 5, plotted in a different format. Reversed field data from the low-field side (LFS) midplane are also included. Red/green curves correspond to favorable/unfavorable x-point topologies with forward field. Orange/blue curves correspond to favorable/unfavorable x-point topologies with reversed field. Top panels show parallel components; bottom panels show $E_r \times B$ components of the perpendicular flow. Positive values indicate flow directed toward the inner divertor. Note the reversal of the ρ-axis in the left panels. On the high-field side (HFS), parallel flows are always directed toward the inner divertor, regardless of x-point location, while $E_r \times B$ flows are directed toward (away) the inner divertor for unfavorable (favorable) drift directions. On the LFS, parallel flow components oppose the direction of $E_r \times B$ components in the scrape-off layer region ($\rho > 0$), but are additive in the closed field line region. Parallel flow components in the LFS are always directed toward (away from) the inner divertor for favorable (unfavorable) drift directions.

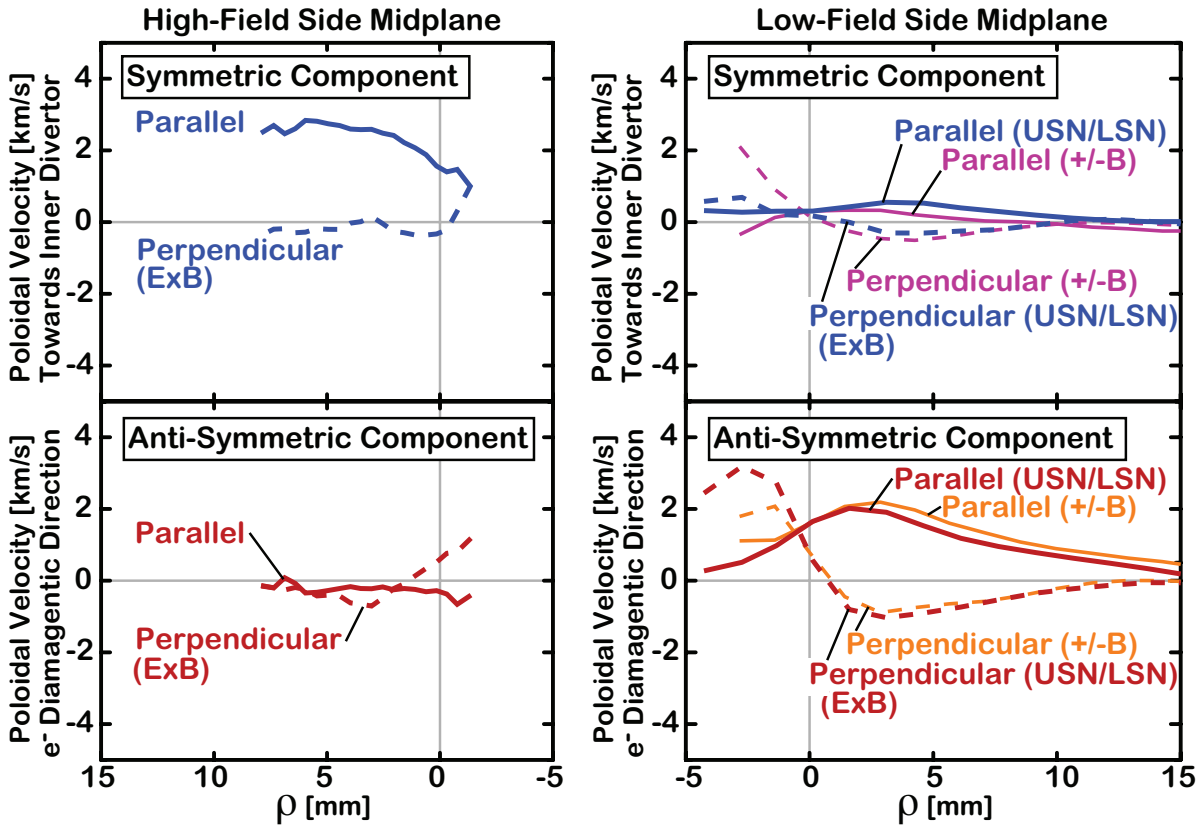

Figure 7. Symmetric (transport-driven) and anti-symmetric (drift-driven) components of parallel and perpendicular ($E_r \times B$) flow on the high-field and low-field side scrape-off layers. The poloidal projection of these components is shown. Positive *symmetric* flow corresponds to flow towards the inner divertor while positive *anti-symmetric* flow corresponds to flow in the electron diamagnetic drift direction. These components are deduced from LSN/USN comparisons with forward magnetic field (red and blue traces) and forward/reversed magnetic field comparisons with LSN topology (purple and orange traces). Flow components obtained from field reversal are very similar to those obtained from topology reversal, indicating that differences in divertor geometry play only a minor role at most.

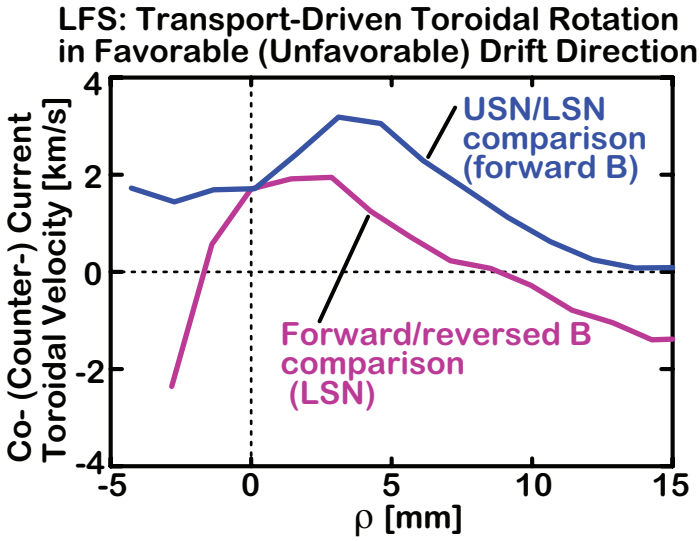

Figure 8. Transport-driven component of toroidal rotation. Symmetric parallel and perpendicular components on the low-field side destructively interfere in the poloidal direction to produce an almost pure toroidal rotation. This is inferred from both a USN/LSN comparison with normal field direction (blue curve) and a forward/reversed B comparison with LSN (purple curve). The transport-driven rotation is in the co-current (counter-current) direction for discharges with favorable (unfavorable) $B \times \nabla B$ drift direction.

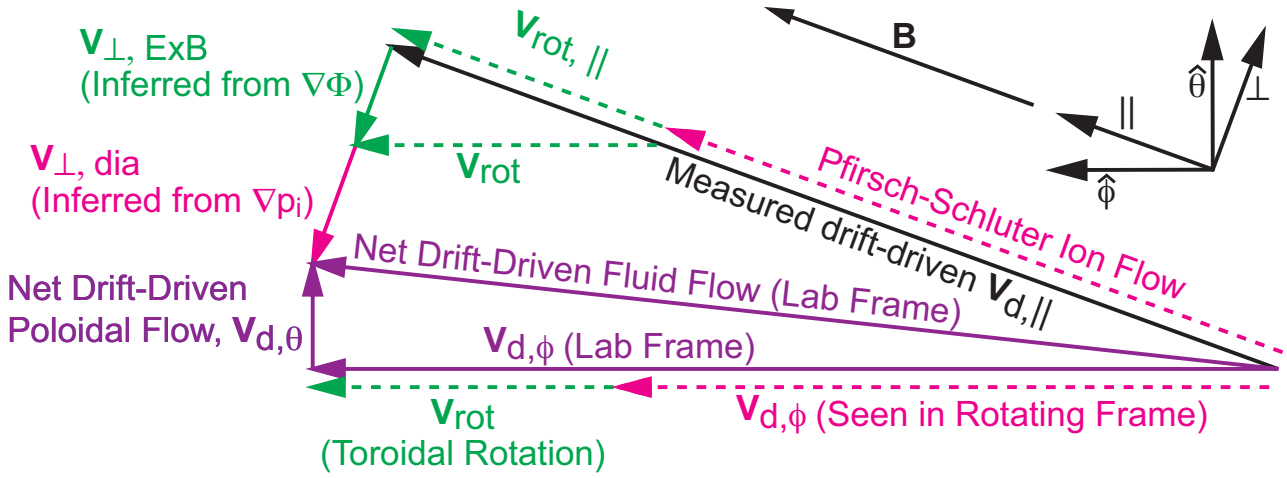

Figure 9. Decomposition of anti-symmetric (drift-driven) plasma flows. Measurement of drift-driven parallel ($V_{d,//}$) and perpendicular ion flows ($V_{\perp\ ExB}$ and $V_{\perp\ dia}$) allow the net drift-driven poloidal ($V_{d,\theta}$) and toroidal ($V_{d,\phi-lab}$) flows to be determined in the laboratory frame. In changing to a reference frame rotating with the plasma, the perpendicular $E_r \times B$ flow ($V_{\perp\ ExB}$) and parallel projection of toroidal rotation velocity ($V_{rot,//}$) are subtracted since, by definition, the radial electric field is zero in this reference frame. The remaining parallel flow is the 'Pfirsch-Schlüter ion flow'. Note that the ion diamagnetic flow and net drift-driven poloidal flow is unchanged by this reference frame transformation.

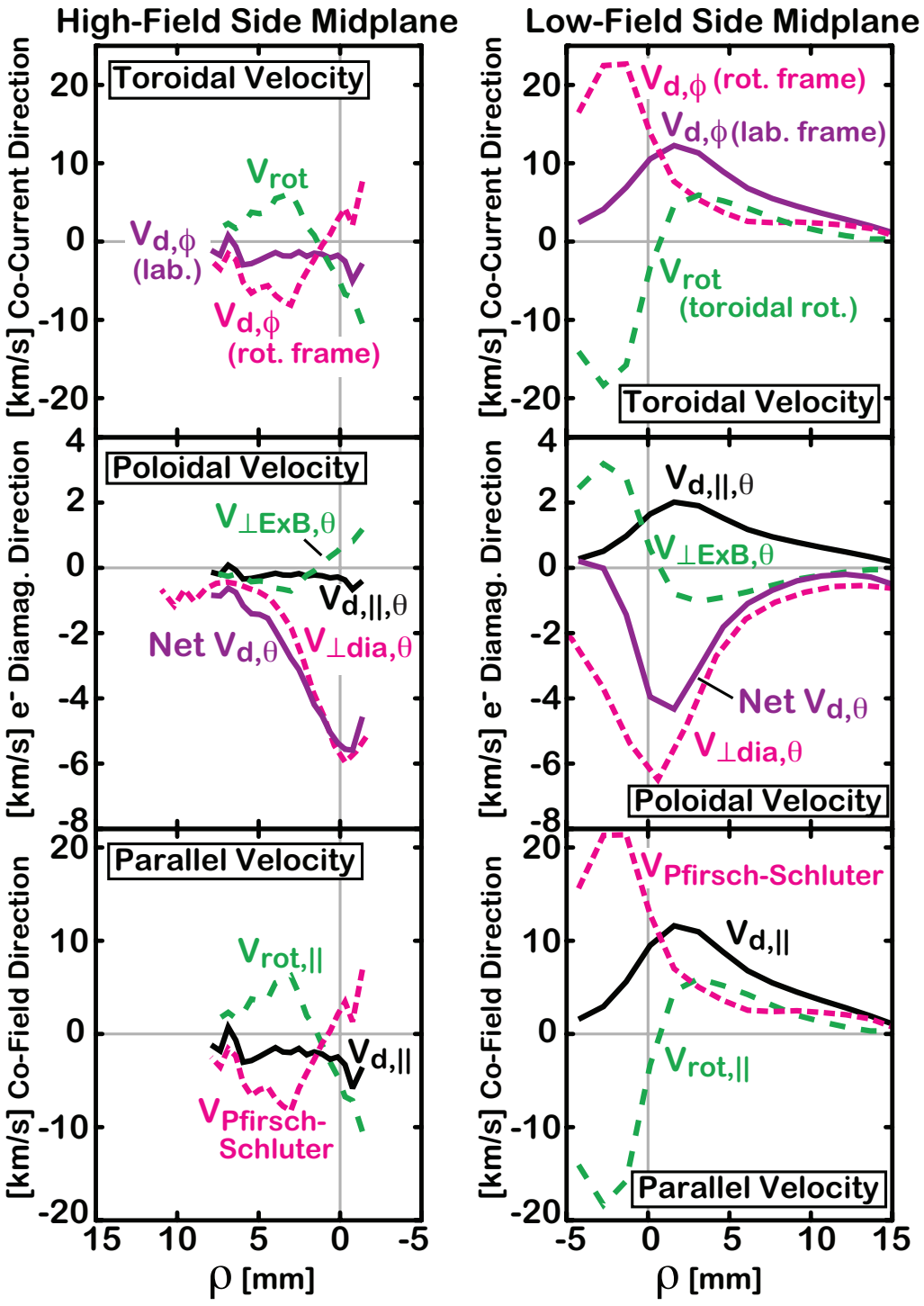

Figure 10. Using the vector manipulations illustrated in Fig. 9, the anti-symmetric (drift-driven) flows observed in Fig. 7 (LSN/USN comparison at forward field) are decomposed into their toroidal, poloidal and parallel flow components, which include toroidal plasma rotation and Pfirsch-Schlüter parallel ion flows.

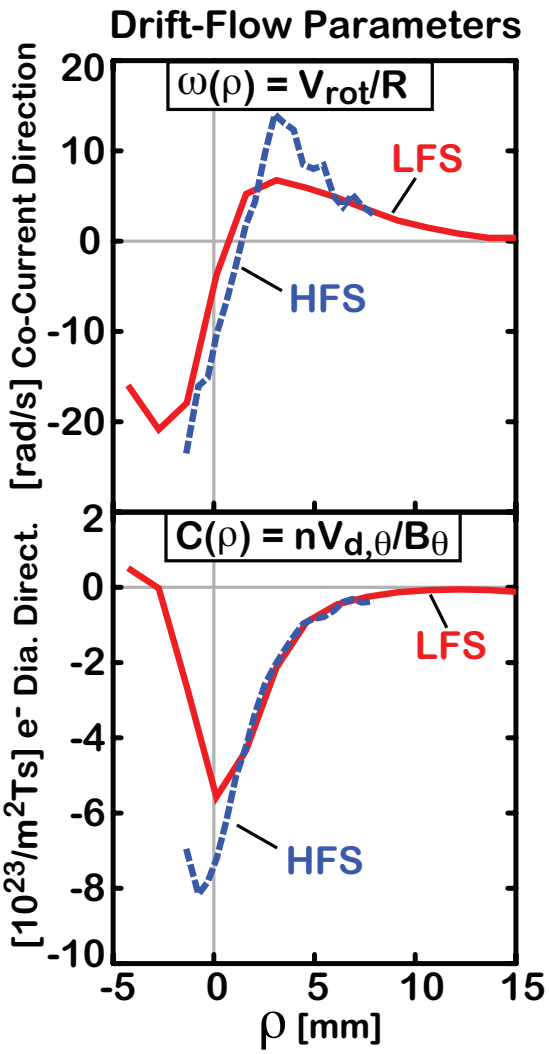

Figure 11. Comparison of toroidal rotation profle, $\omega(\rho)$, and poloidal flow circulation profile, $C(\rho)$, computed from HFS and LFS anti-symmetric (drift-driven) flow data. Both parameters are observed to have roughly the same profile at each poloidal location, as required theoretically for the plasma potential to be a flux function and for the overall drift-driven flow field to be divergence-free.

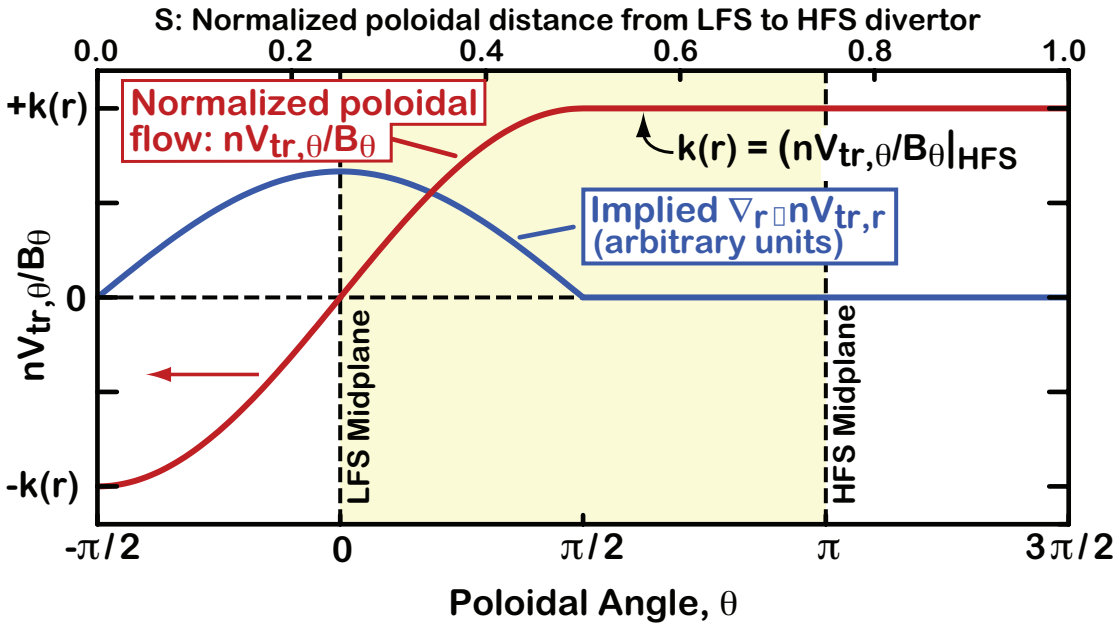

Figure 12. Model functions are used to approximate the poloidal variation in transport-driven poloidal flows (red) and corresponding radial divergence in radial transport fluxes (blue). Note the discontinuity at $\theta = -\pi/2$, corresponding to the x-point location. While this feature requires the circulating flow to return by some unspecified process near the x-point and/or divertor regions, we do not address this question here. Rather, we restrict our attention to the domain (yellow) that extends from the LFS midplane ($\theta = 0$) to the HFS midplane ($\theta = \pi$) to test if the measured poloidal and radial fluxes are consistent with overall particle continuity.

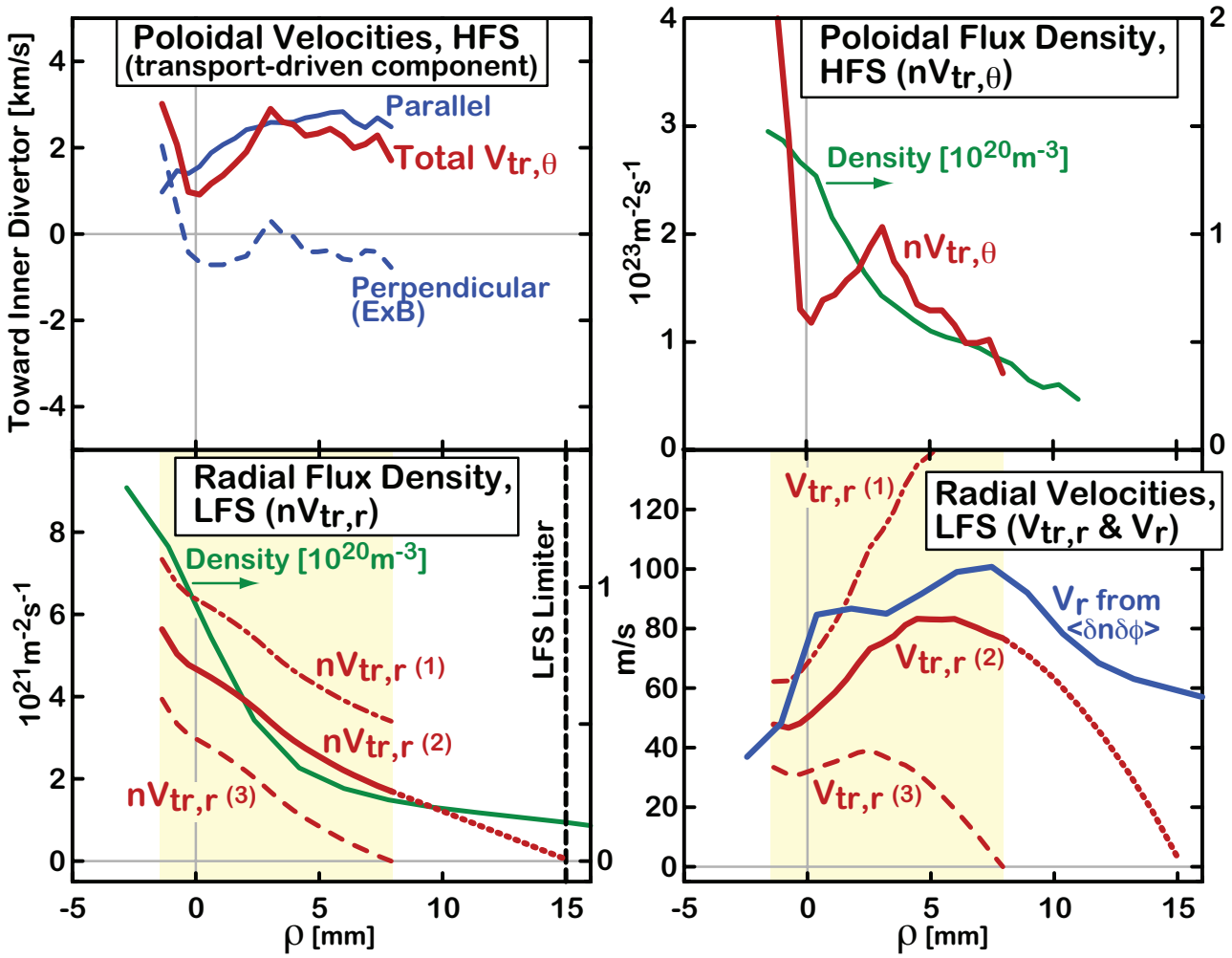

Figure 13. Symmetric (transport-driven) poloidal flow velocities measured on the HFS midplane (upper left panel) are used to construct a poloidal flux density profile there (upper right panel). This is inputted to a ballooning-like particle continuity model [Eqs. (13)-(17), evaluated over the computational domain highlighted in yellow], yielding quantitative estimates of the required radial particle flux density profiles on the LFS (lower left panel). Case #2 extrapolates to a radial flux of zero at the LFS limiter, the most plausible case. Corresponding radial velocities on the LFS are shown in the lower right panel (red curves). An independent measure of the radial transport fluxes on the LFS midplane, i.e., the fluctuation-induced particle fluxes ($V_r = \Gamma_r / n$, blue curve), yields a remarkably consistent profile.

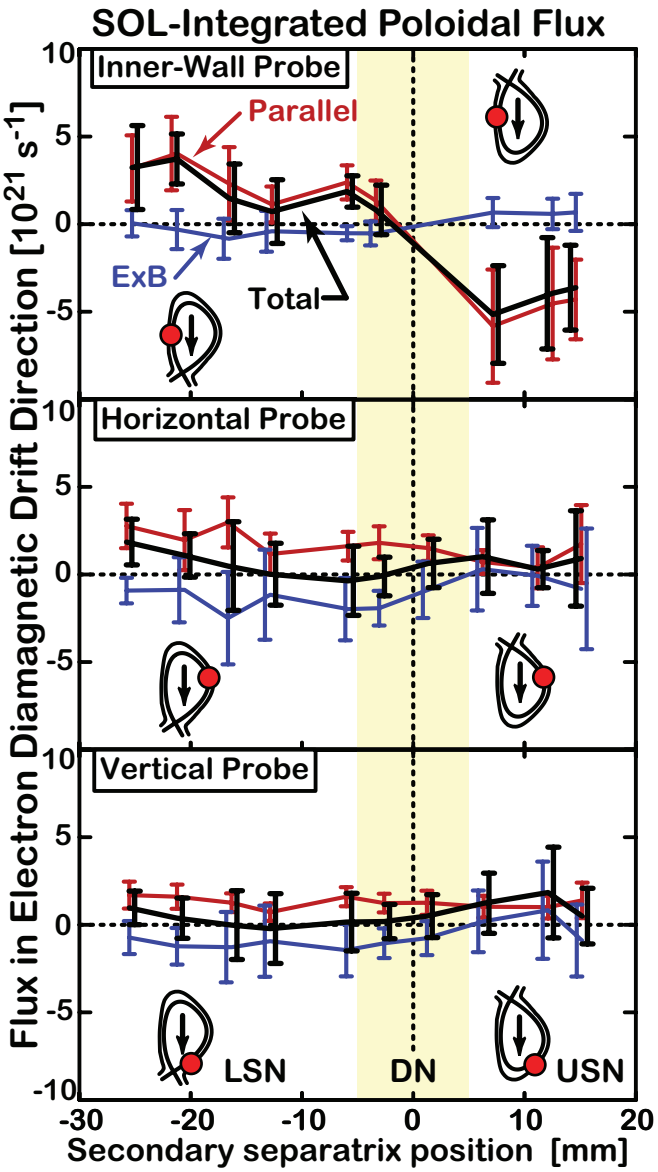

Figure 14. Net poloidal particle flux [Γ_θ, computed from Eq. (18)] and its components (parallel flow in red, $E_r \times B$ flow in blue) passing inner-wall, horizontal and vertical probe locations as a function of magnetic x-point balance. Horizontal axis corresponds to distance between primary and secondary separatrix locations, mapped to the outer midplane. Negative values indicating LSN, positive values USN. Data are obtained from discharges with normal current (0.8 MA) and field (5.4 T) directions, binned according to secondary separatrix location. Error bars indicate plus and minus one standard deviation about the mean value. Positive flux is in the electron diamagnetic drift direction (i.e., towards the inner divertor for LSN). The $E_r \times B$ flow contribution does not affect the overall poloidal particle flux on the HFS scrape-off layer; the poloidal flux at this location is unambiguously directed towards the inner divertor. $E_r \times B$ flows largely cancel parallel flows on the LFS scrape-off layer, leading to a co-current toroidal plasma rotation near the LFS midplane that is stronger in favorable (LSN) versus unfavorable (USN) drift topologies.

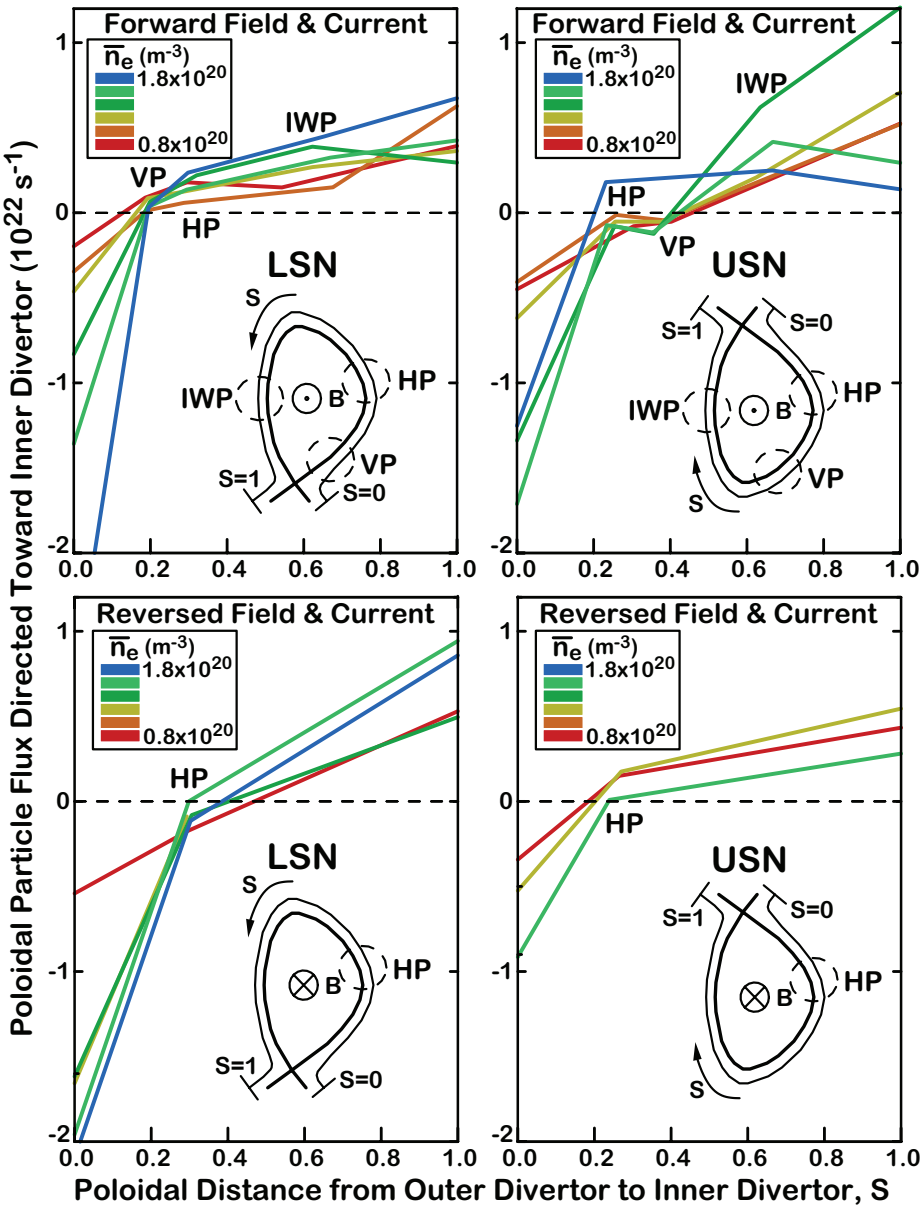

Figure 15. Net poloidal particle flux, Γ_θ, measured by all probe systems, plotted as a function of the normalized distance from outer divertor to inner divertor for normal field direction (top panels) and reversed field direction (bottom panels). Γ_θ is computed using Eq. (18) for scanning probes and from ion saturation currents measured on divertor surfaces. Positive fluxes are directed towards the inner divertor. Left panels shows results for a lower single-null topology, right panels show upper single-null. Data are binned according to density as indicated by color scale. Each line in the upper panels is constrained by five measurements locations, corresponding to two divertor probe arrays and the three scanning probes. Lines in the lower plots are constrained at only three locations. While the reversed field data set is very sparse, it indicates that the overall trends swap with USN/LSN, in accordance with the reversal of the direction of the $\boldsymbol{B} \times \nabla B$ drift. Over a wide range of conditions, the poloidal flux passing through the HFS midplane is comparable to or exceeds the ion flux arriving on the inner divertor target.

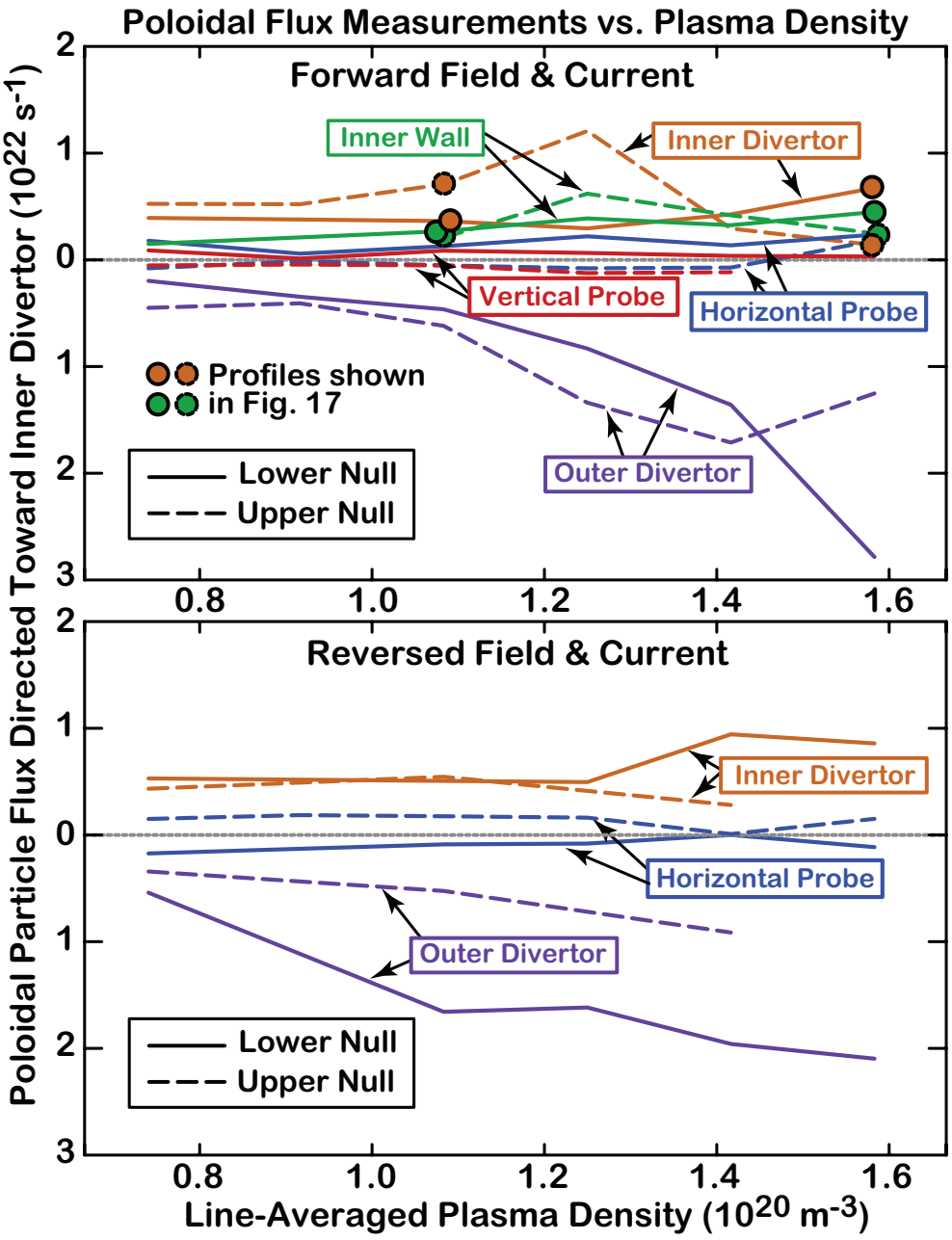

Figure 16. Net poloidal particle flux, Γ_θ, at different poloidal locations, plotted as a function of line-averaged plasma density. Data from forward toroidal field and current direction are shown in the top panel, reversed direction in the bottom panel. Solid lines indicate lower single-null topology, dashed lines indicate upper single-null.

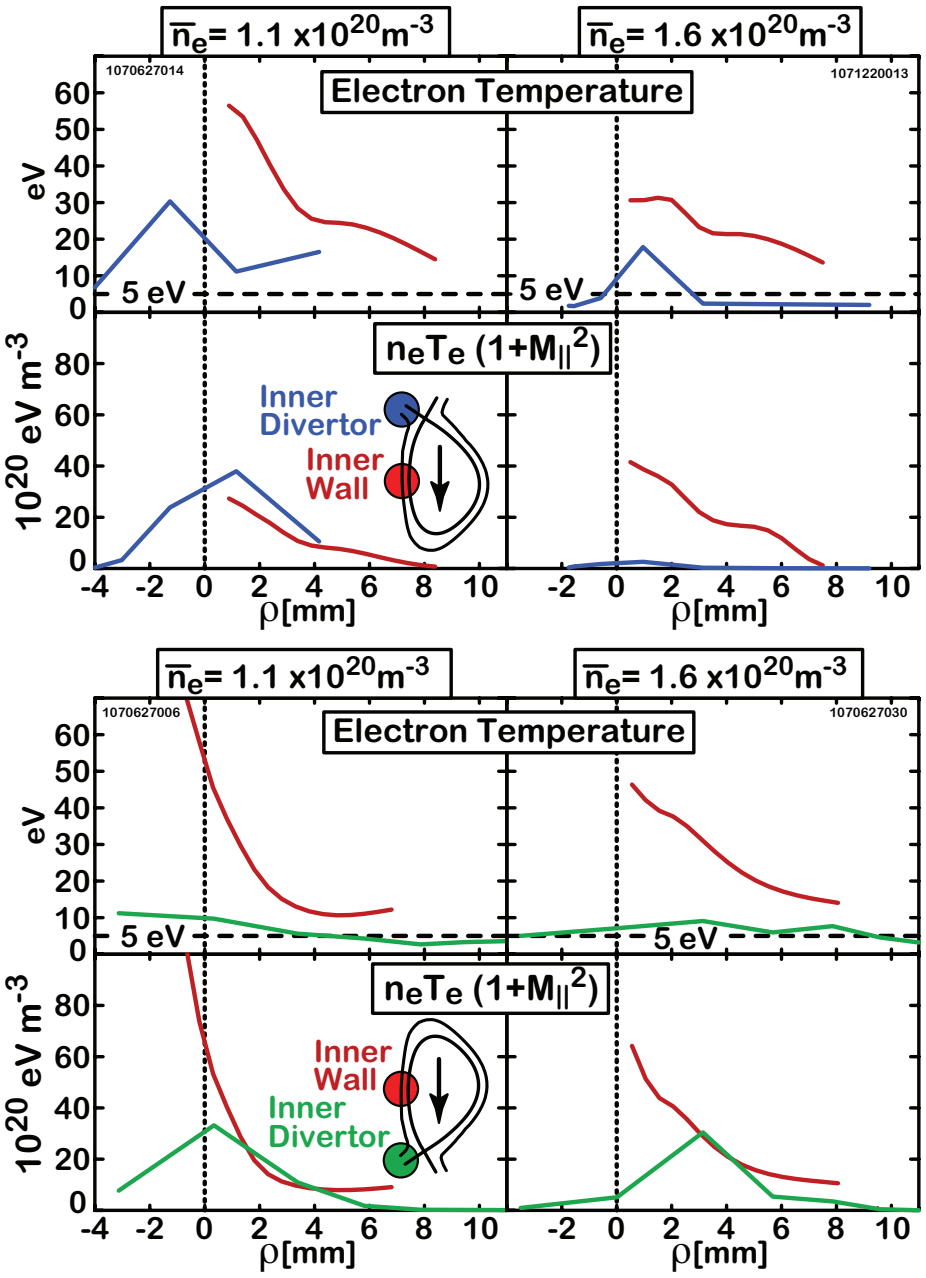

Figure 17. Electron temperature and total pressure (kinetic + ram) profiles measured at the Inner Wall and Inner Divertor locations in USN (top panels) and LSN conditions (bottom panels) at two different line-averaged densities. These discharges had forward field (5.4 T) and current (0.8 MA) corresponding to data points marked with circles in Fig. 16. Left columns show moderate density discharges: These achieve approximate pressure balance between Inner Wall and Inner Divertor locations, regardless of LSN/USN topology. Right columns show high density discharges: Large inner divertor pressure losses (~detachment) occur in USN while pressure loss is seen only near the strike-point (ρ = 0) in LSN. Despite these clear differences in divertor conditions and their variation with plasma density, the poloidal flux at the Inner Wall location shows only small variations with plasma density (see Fig. 16).

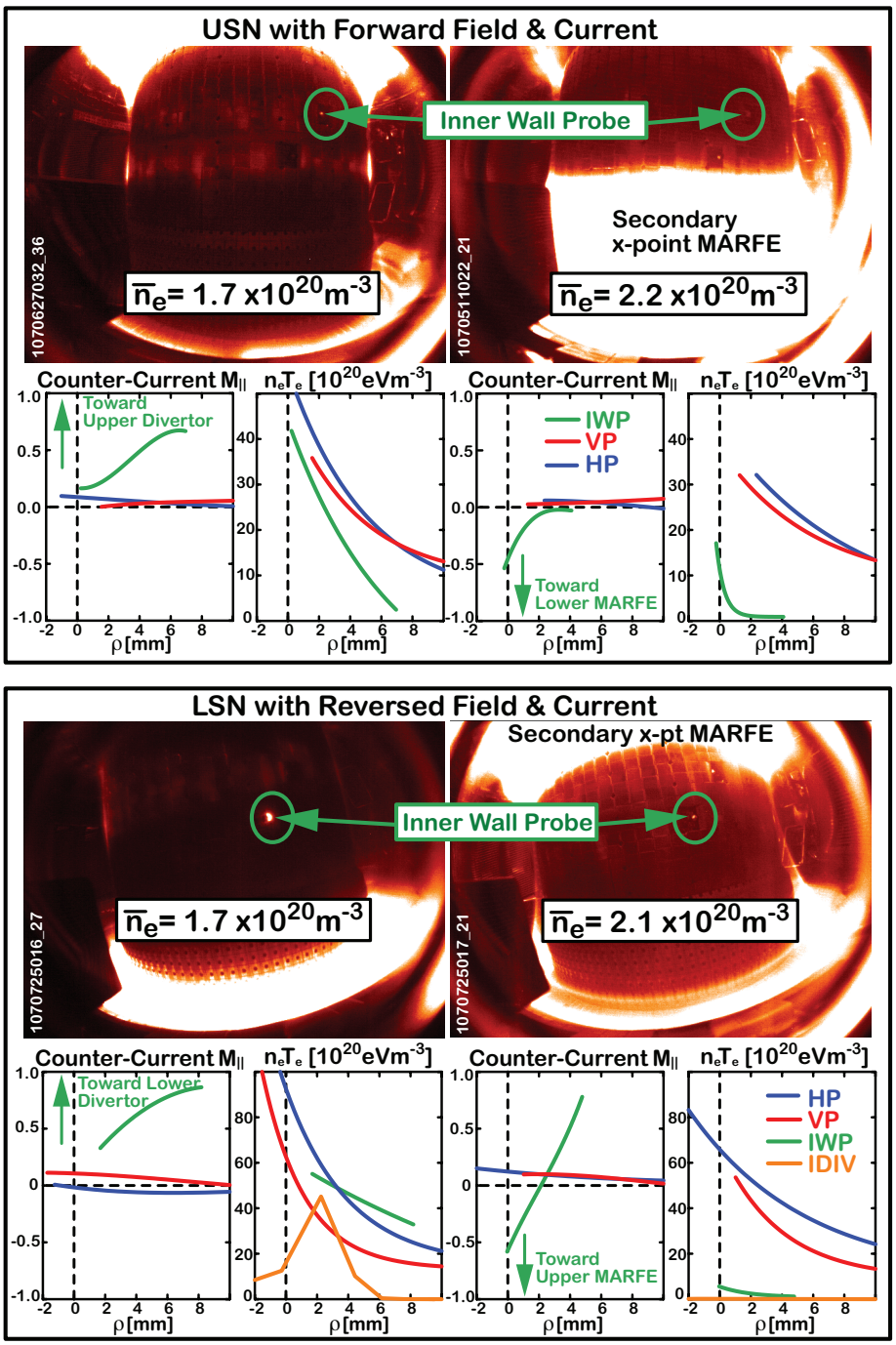

Figure 18. Comparison of electron pressure profiles and flows on HFS SOL in discharges with and without secondary x-point MARFEs. The top half of the figure shows similar USN discharges in normal field: left side without MARFE, right side with MARFE at higher density. Below each picture are the corresponding measured parallel plasma flow Mach numbers (positive indicates counter-current direction) and pressures from horizontal (HP), vertical (VP) and inner-wall probes (IWP). The bottom half of the figure shows the same comparison for LSN discharges in reversed field, including lower inner divertor (IDIV) electron pressure profiles.

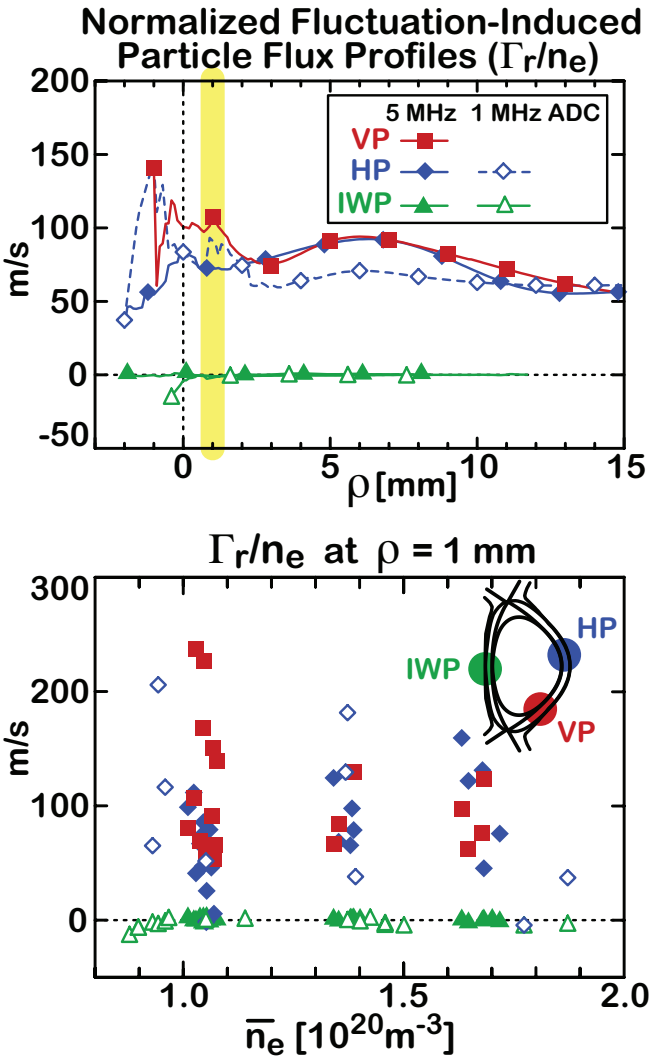

Figure 19. Measurements of fluctuation-induced radial particle flux density, normalized to local plasma density (Γ_r / n_e). Cross-field profiles of Γ_r / n_e at the three scanning probe locations are shown in the top panel. These were obtained from averaging Γ_r / n_e profiles over the full range of densities shown in the bottom panel. Open symbols are from data sampled at 1 MHz, filled symbols at 5 MHz. The bottom panel shows individual Γ_r / n_e measurements at the location of ρ = 1 mm (vertical yellow line in top panel), ordered according to line-averaged plasma density. The data do not depend on x-point location (USN versus LSN).

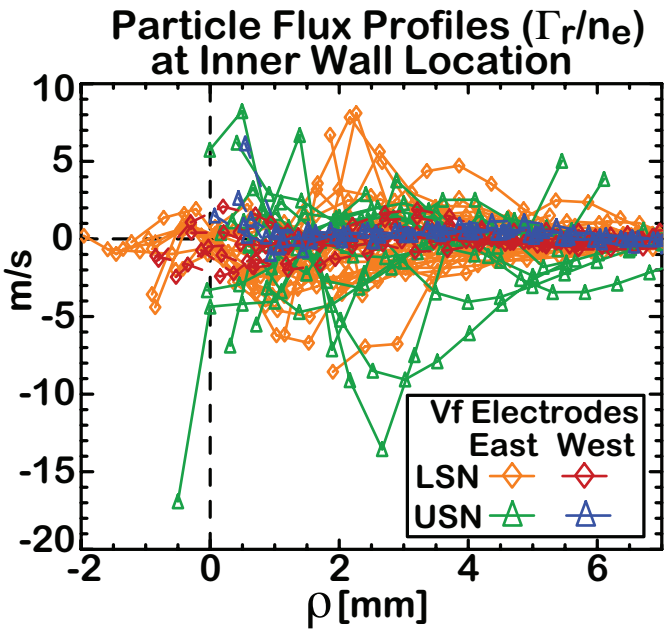

Figure 20. Normalized fluctuation-induced radial flux profiles (Γ_r / n_e) measured by the Inner Wall Scanning probe on individual scans. The data shown in Fig. 19 were obtained from averaging these profiles. Measurements with the east electrodes floating (NE, SE – see Fig. 4) are similar to those with the west electrodes floating (NW, SW), although the scatter is reduced in the latter case. In any case, Γ_r / n_e at the inner wall location is statistically zero to within the standard deviation (+/- ~2 m/s) derived from the sample variance.

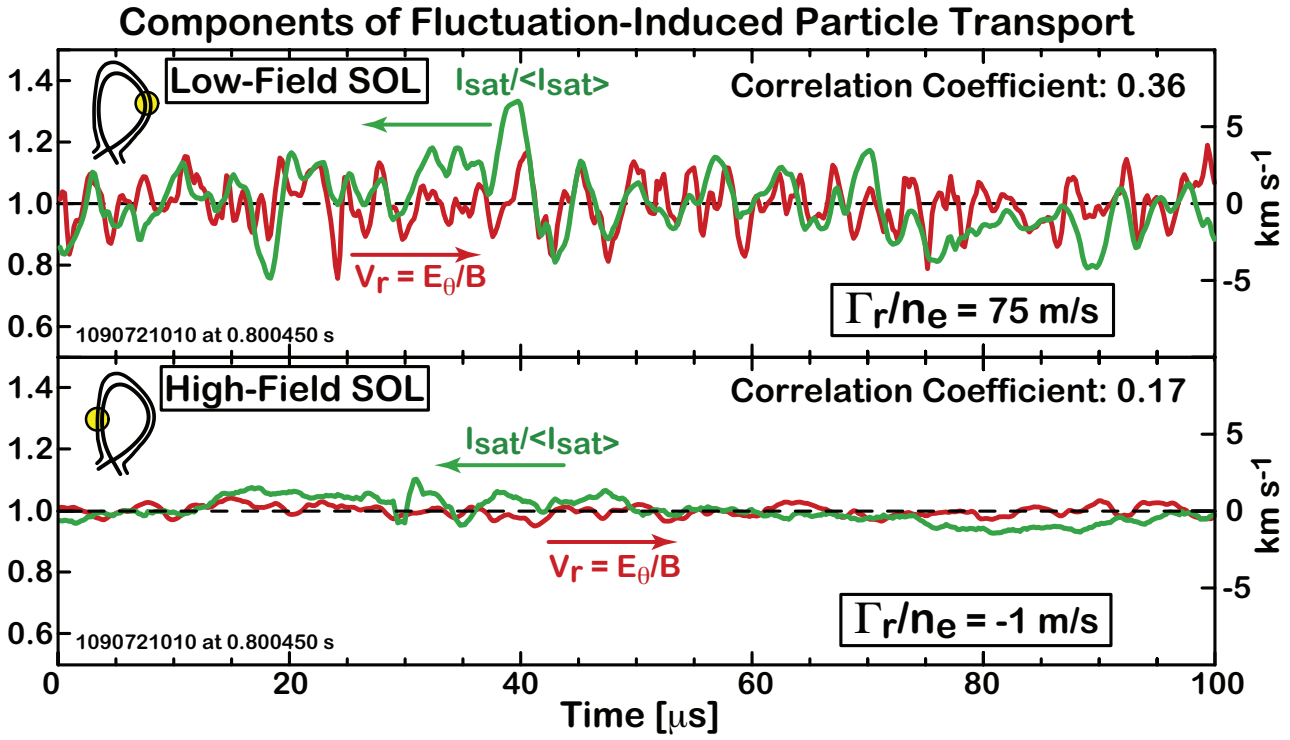

Figure 21. Representative fluctuation time series in the LFS (top panel) and HFS (bottom panel) scrape-off layers of normalized ion saturation current ($I_{sat}/\langle I_{sat}\rangle$) and radial $E \times B$ velocity ($V_r = E_\theta / B$), computed from horizontal and inner-wall scanning probes. In these cases, E_θ is computed from the NW and SW electrodes (floating mode) while I_{sat} is the total ion current collected on the NE and SE electrodes (ion saturation mode). Fluctuations in density and potential on the LFS are higher in amplitude than on the HFS and are correlated so as to produce a net positive time-averaged radial particle flux. Fluctuation amplitudes on the HFS are smaller and are weakly correlated, resulting in essentially a zero time-averaged radial particle flux.

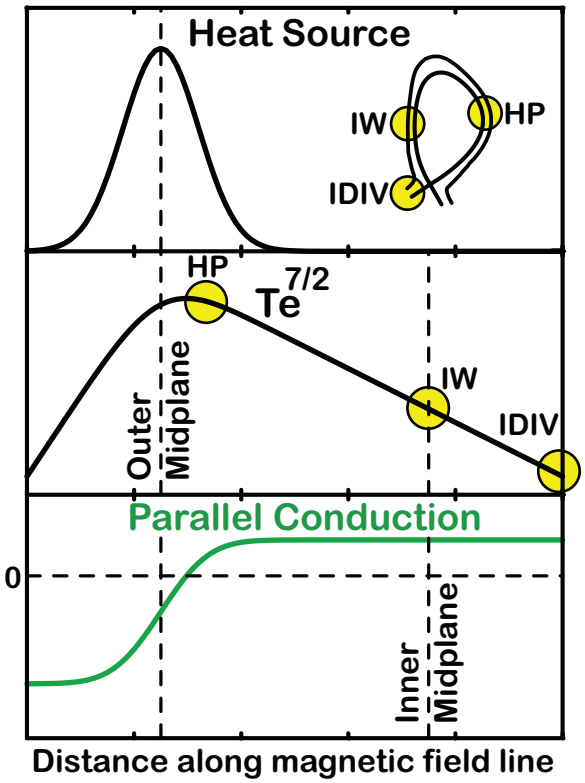

Figure 22. A simplified heat flow model is used to estimate the parallel heat conduction component in the HFS scrape-off layer [$q_{cond} = -\kappa_{\|}^{e}\nabla_{\|}T_r$]. On the basis of the particle flux measurements in section 5, Heat loss is assumed to occur entirely in the LFS scrape-off layer (top panel). If parallel conduction dominated the poloidal heat flow, the quantity $T_e^{7/2}$ would vary linearly with distance along a field line that connects outer-midplane and inner-midplane regions (middle panel), producing to a constant heat flux density (bottom panel). Straight lines are therefore drawn between probe measurements of $T_e^{7/2}$ at the horizontal (HP), inner-wall (IW) and inner divertor probe locations (IDIV); $\nabla_{\|}T_e^{7/2}$ is taken to be the average slope of these lines from which q_{cond} is estimated.

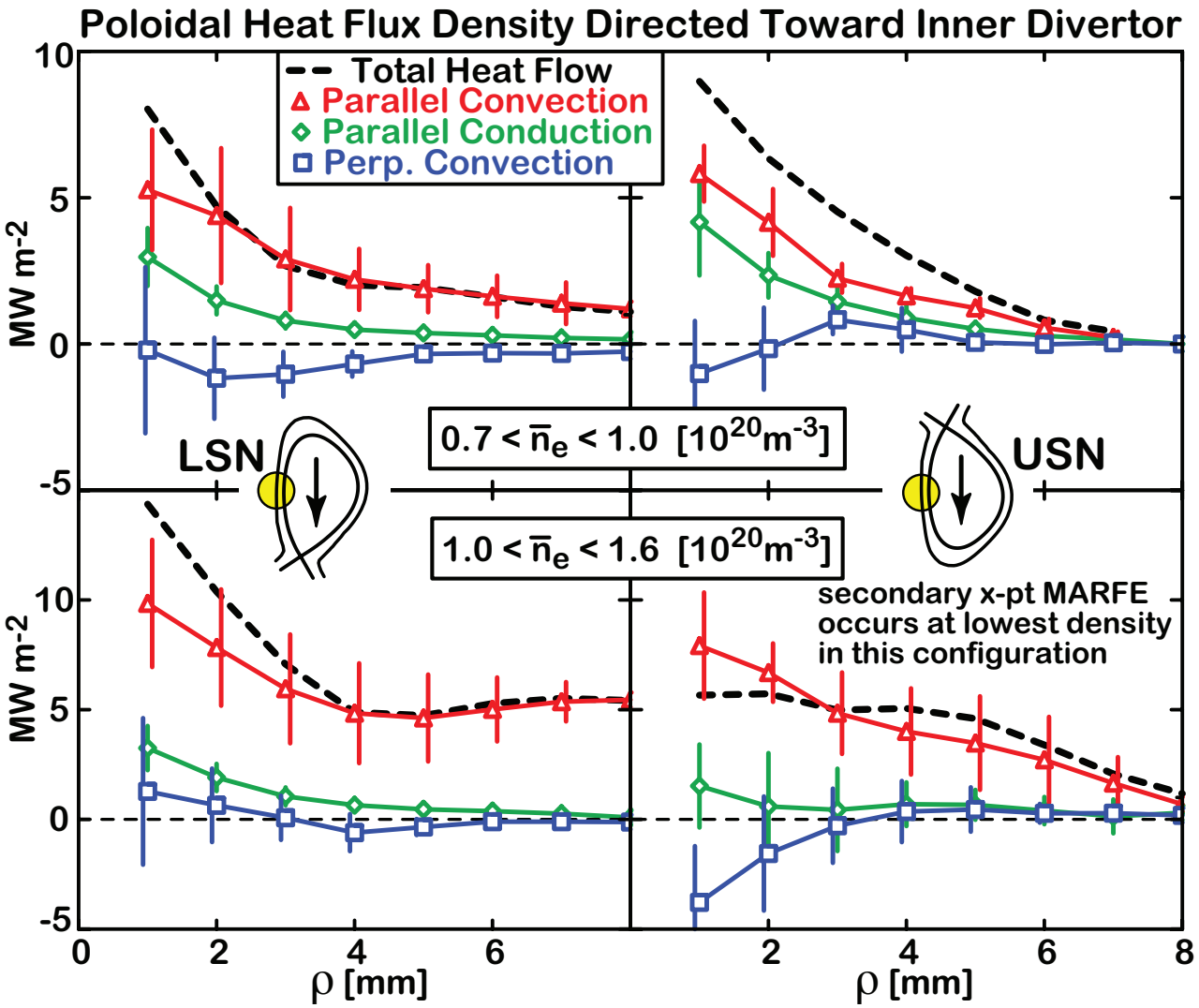

Figure 23. Poloidal heat flux density profiles at the location of the inner-wall scanning probe, evaluated from Eq. (21). The net poloidal heat flux (black dashed line) is the sum of the parallel convection (red), parallel conduction (green) and perpendicular convection components (blue). Data from low density discharges are shown in the top panels, moderate density in the lower panels. LSN discharges are shown on the left, USN on the right. Secondary x-pt MARFEs tend to occur at lower $\bar{n}_e$ in USN compared to LSN. Measurements shown in lower right panel suggest an explanation: at high densities, $E_r \times B$ heat convection strongly opposes heat flow to the inner divertor in this configuration.

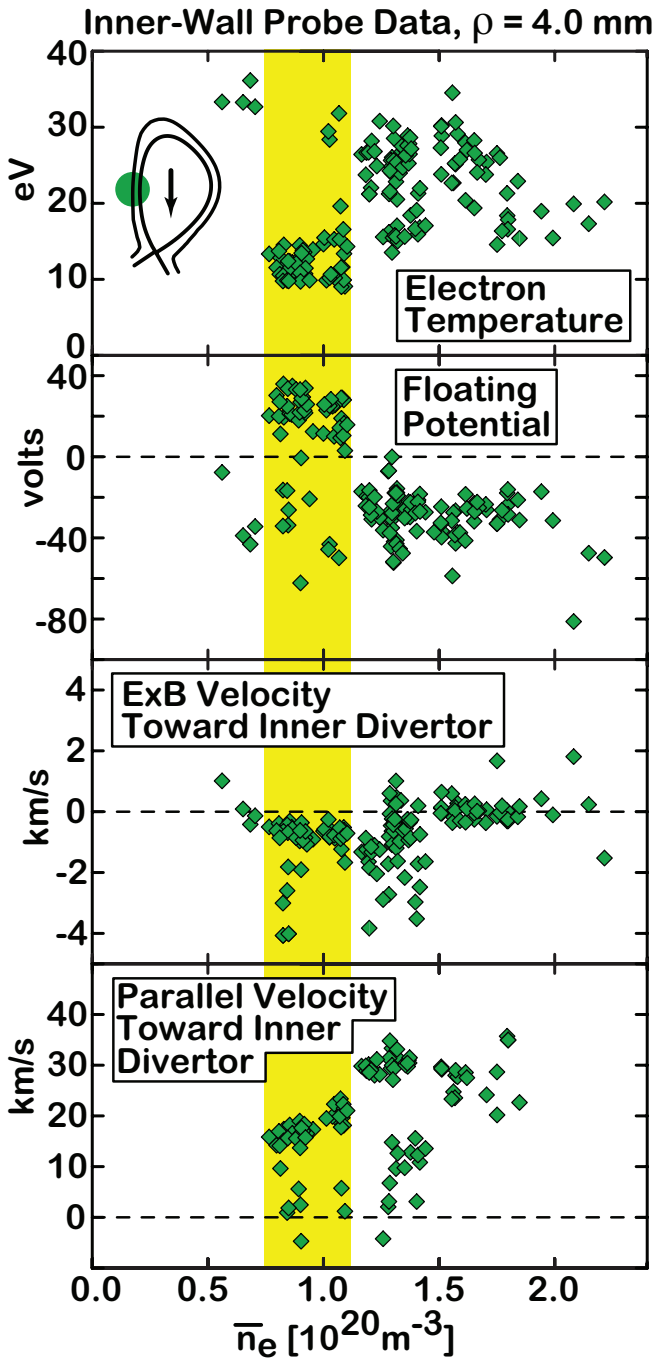

Figure 24. Plasma conditions measured from individual plunges of the inner-wall scanning probe at a location of ρ = 4 mm. At low line-averaged plasma densities, T_e measurements are seen drop to low values – an initially puzzling result (see top panel, yellow banded region). Floating potentials also rise, consistent with plasma potential ($\sim V_f + 2.7T_e$) remaining approximately uneffected (second panel). These conditions also favor strong $E_r \times B$ convection *away* from the inner divertor (third panel) and weaker parallel convection toward the inner divertor (bottom panel). Thus the reduction in T_e is potentially explained as being the consequence of a reduction in convected energy flows in the HFS scrape-off layer.